





DUDLEY KNOX LIBRARY  
NAVAL POSTGRADUATE SCHOOL  
MONTEREY, CALIFORNIA 93943-6002





# NAVAL POSTGRADUATE SCHOOL

Monterey, California



## THESIS

CO<sub>2</sub> PULSED LASER DAMAGE MECHANISM AND  
PLASMA EFFECTS  
(FOCUSED BEAM)

by

Richard Lynn Weston

December 1986

Thesis Advisor

F. Schwirzke

Approved for public release; distribution is unlimited

T233050



## REPORT DOCUMENTATION PAGE

1a REPORT SECURITY CLASSIFICATION Unclassified			1b RESTRICTIVE MARKINGS	
2a SECURITY CLASSIFICATION AUTHORITY			3 DISTRIBUTION/AVAILABILITY OF REPORT Approved for public release; distribution is unlimited.	
2b DECLASSIFICATION/DOWNGRADING SCHEDULE			5 MONITORING ORGANIZATION REPORT NUMBER(S)	
4 PERFORMING ORGANIZATION REPORT NUMBER(S)			7a NAME OF MONITORING ORGANIZATION Naval Postgraduate School	
6a NAME OF PERFORMING ORGANIZATION Naval Postgraduate School		6b OFFICE SYMBOL (if applicable) 61	7b ADDRESS (City, State, and ZIP Code) Monterey, California 93943-5000	
6c ADDRESS (City, State, and ZIP Code) Monterey, California 93943-5000		9 PROCUREMENT INSTRUMENT IDENTIFICATION NUMBER		
8a NAME OF FUNDING/SPONSORING ORGANIZATION		8b OFFICE SYMBOL (if applicable)	10 SOURCE OF FUNDING NUMBERS	
8c ADDRESS (City, State, and ZIP Code)		PROGRAM ELEMENT NO	PROJECT NO	TASK NO
		WORK UNIT ACCESSION NO		
11 TITLE (Include Security Classification) CO <sub>2</sub> PULSED LASER DAMAGE MECHANISM AND PLASMA EFFECTS (FOCUSED BEAM) UNCLASSIFIED				
12 PERSONAL AUTHOR(S) Weston, Richard L.				
13a TYPE OF REPORT Master Thesis		13b TIME COVERED FROM TO		15 PAGE COUNT 83
14 DATE OF REPORT (Year, Month, Day) 1986 December				
16 SUPPLEMENTARY NOTATION				
17 COSATI CODES			18 SUBJECT TERMS (Continue on reverse if necessary and identify by block number)	
FIELD	GROUP	SUB-GROUP	CO <sub>2</sub> Pulsed Laser, Unipolar arcing, Plasma effects, Damage threshold for AISI SS 304.	
19 ABSTRACT (Continue on reverse if necessary and identify by block number)				
<p>An experiment was conducted (at NPS) with AISI SS 304 stainless steel targets, in a 10<sup>-6</sup> Torr vacuum using a CO<sub>2</sub> TEA high energy, pulsed laser with a beam focused to 1 cm<sup>2</sup>. An investigation of the laser damage mechanism was conducted. The power density required for onset of plasma formation and the start of surface damage were determined.</p> <p>Targets were polished to 0.25 micron finish. Target specimens were examined using a scanning electron microscope to determine damage features of micron size dimensions. Experimental results confirmed that the surface damage was confined solely to unipolar arcing and thermal effects resulting from the arcing process. Several targets were cross-sectioned and chemically etched to determine changes in the microstructure of the stainless steel. At high power densities, the surface was heated sufficiently to cause a change in the stainless steel</p>				
20 DISTRIBUTION/AVAILABILITY OF ABSTRACT <input checked="" type="checkbox"/> UNCLASSIFIED/UNLIMITED <input type="checkbox"/> SAME AS RPT <input type="checkbox"/> DTIC USERS			21 ABSTRACT SECURITY CLASSIFICATION Unclassified	
22a NAME OF RESPONSIBLE INDIVIDUAL F. Schwirzke			22b TELEPHONE (Include Area Code) (408) 646-2487	22c OFFICE SYMBOL 61sw

Cont. of block 19

from Austenite to Austenite and Ferrite. The localized change in the microstructure confirmed that the energy deposition from the plasma was confined to the arcing craters. The power density for onset of plasma formation and unipolar arcing was determined to be  $0.41 \text{ MW/cm}^2$ .

A Sequential Unipolar Arcing Model which incorporated the details of the refined Schwirzke Model was developed. The qualitative predictions of the model were confirmed by the experimental results.



Approved for public release; distribution is unlimited.

CO<sub>2</sub> Pulsed Laser Damage Mechanism and  
Plasma Effects  
(Focused Beam)

by

Richard Lynn Weston  
Lieutenant, United States Navy  
B.S. Computer Science, University of Minnesota, 1979

Submitted in partial fulfillment of the  
requirements for the degree of

MASTER OF SCIENCE IN ENGINEERING SCIENCE

from the

NAVAL POSTGRADUATE SCHOOL  
December 1986

## ABSTRACT

An experiment was conducted (at NPS) with AISI SS 304 stainless steel targets, in a  $10^{-6}$  Torr vacuum using a  $\text{CO}_2$  TEA high energy, pulsed laser with a beam focused to  $1 \text{ cm}^2$ . An investigation of the laser damage mechanism was conducted. The power density required for onset of plasma formation and the start of surface damage were determined.

Targets were polished to 0.25 micron finish. Target specimens were examined using a scanning electron microscope to determine damage features of micron size dimensions. Experimental results confirmed that the surface damage was confined solely to unipolar arcing and thermal effects resulting from the arcing process. Several targets were cross-sectioned and chemically etched to determine changes in the microstructure of the stainless steel. At high power densities, the surface was heated sufficiently to cause a change in the stainless steel from Austenite to Austenite and Ferrite. The localized change in the microstructure confirmed that the energy deposition from the plasma was confined to the arcing craters. The power density for onset of plasma formation and unipolar arcing was determined to be  $0.41 \text{ MW/cm}^2$ .

A Sequential Unipolar Arcing Model which incorporated the details of the refined Schwirzke Model was developed. The qualitative predictions of the model were confirmed by the experimental results.

## TABLE OF CONTENTS

I.	INTRODUCTION .....	12
II.	BACKGROUND AND THEORY .....	14
	A. INTRODUCTION .....	14
	B. DEFINITIONS .....	14
	1. Desorption .....	14
	2. Sputtering .....	14
	3. Thermal Evaporation .....	15
	4. Energy Coupling .....	15
	5. Plasma .....	17
	C. UNIPOLAR ARCING .....	20
	1. Robson-Thonemann Model .....	20
	2. Schwirzke-Taylor Model .....	21
III.	EXPERIMENTAL METHOD .....	35
	A. INTRODUCTION .....	35
	B. EXPERIMENTAL APPARATUS .....	35
	1. Laser .....	35
	2. Vacuum Chamber .....	36
	3. NaCl Windows .....	38
	4. Pyroelectric Energy Meters .....	38
	5. Infrared Detector .....	39
	6. Optics .....	39
	7. Scanning Electron Microscope .....	40
	C. LASER FACILITY .....	40
	D. PROCEDURES .....	41
	1. Target Preparation .....	41
	2. Target Alignment .....	42
	3. Power Density .....	42

4.	Determination of Plasma Onset .....	43
5.	Evaluation of Target Surface Damage .....	43
E.	EXPERIMENTAL ERROR .....	43
F.	EXPERIMENTAL LIMITATIONS .....	44
1.	Beam Nonuniformities .....	44
2.	Laser Pulse Duration .....	44
3.	ZnSe Vacuum Chamber Window .....	45
4.	Target Orientation .....	45
5.	Laser Chill Water Unit .....	45
6.	Vacuum Chamber Mechanical Pump Exhaust .....	45
IV.	EXPERIMENTAL RESULTS .....	46
A.	DETERMINATION OF PLASMA ONSET IN VACUUM .....	46
B.	BEAM INACCURACIES .....	46
C.	TARGET SURFACE DAMAGE .....	47
1.	High Power Densities .....	47
2.	Thermal Effects .....	51
3.	Low Power Density .....	55
D.	ZINC SELENIDE WINDOW .....	61
E.	DISCUSSION OF RESULTS .....	63
1.	Introduction .....	63
2.	Qualitative Comparison of Previous Results .....	63
3.	Comparison of Focused and Unfocused Beam Experimental Results .....	64
V.	CONCLUSIONS AND RECOMMENDATIONS .....	65
A.	QUALITATIVE COMPARISON OF EXPERIMENTAL RESULTS WITH THE THEORETICAL MODEL .....	65
B.	PLASMA FORMATION POWER DENSITY THRESHOLD .....	65
C.	RECOMMENDATIONS .....	66
1.	Facility Improvements .....	66
2.	Possible Future Research .....	66
APPENDIX A:	LUMONICS TE-822 HP CO <sub>2</sub> LASER OPERATING PROCEDURE .....	67



APPENDIX B: TABLES .....	74
LIST OF REFERENCES .....	80
INITIAL DISTRIBUTION LIST .....	82

## LIST OF TABLES

1.	LASER PULSE ENERGY REPEATABILITY (27 KV/7100 ENERGY METER) .....	74
2.	LASER PULSE ENERGY REPEATABILITY (27 KV/3232 ENERGY METER) .....	75
3.	LASER PULSE ENERGY REPEATABILITY (28 KV/7100 ENERGY METER) .....	76
4.	LASER PULSE ENERGY REPEATABILITY (28 KV/7100 ENERGY METER) .....	77
5.	LASER PULSE ENERGY REPEATABILITY (33 KV/7100 ENERGY METER) .....	78
6.	ONSET OF PLASMA FORMATION DATA FOR SS304 TARGETS IRRADIATED IN A VACUUM .....	79

## LIST OF FIGURES

2.1	Sputtering Yield as a Function of Incident Energy for Stainless Steel and Various Incident Ions. Dashed Lines are for Single Energies Solid Lines are Averaged Energies Assuming a Maxwellian Distribution at Normal Incidence .....	16
2.2	Reflectivity vs Time for 10.6 Micron Radiation for SS 304 .....	17
2.3	Electron - Ion Flow from Plasma to a Metal Surface Prior to Cathode Spot Formation .....	22
2.4	Electron - Ion Flow from a Plasma to a Metal Surface After Arcing has Initiated .....	23
2.5	Schwirzke-Taylor Unipolar Arc Model .....	24
2.6	Onset of Plasma Formation .....	25
2.7	Electric Field and Floating Potential Formation .....	27
2.8	Local Electric Field Enhancement at Whisker Tip .....	31
3.1	Experimental Arrangement .....	37
3.2	4.55 $\mu$ sec FWHM Pulse Width for Standard Long Pulse Gas Settings Horizontal Axis - 2 $\mu$ sec per division Vertical Axis 0.1 Volts per Division .....	38
4.1	Plasma Plume from Laser/Target Surface Interaction (High Power Density) .....	48
4.2	Hot Spot Damage at 41.4x Magnification with the SEM .....	48
4.3	Center of Beam Hot Spot at 326x The Large Crater at Upper Right was 125 $\mu$ m Across Cathode Spot was 14 $\mu$ m .....	50
4.4	Center of Hot Spot, Craters Overlap and Run Together .....	50
4.5	Crater Size and Density Near the Edge of the Hot Spot .....	51
4.6	Unirradiated Surface 1250x .....	52
4.7	Unirradiated Surface After Etching, Optical Microscope 500x .....	53
4.8	Thermal Effects in Beam Hot Spot SEM 346 .....	53
4.9	Thermal Effects in Beam Hot Spot SEM 1340x .....	54

4.10	Thermal Effects in Beam Hot Spot, After Etching Optical Microscope 500x .....	54
4.11	Etched Craters at Edge of Hot Spot Localized Energy Deposition Caused Local Phase Change Optical Microscope 500x .....	55
4.12	Typical Arc Crater at 0.559 MW/cm <sup>2</sup> 1390x .....	56
4.13	Typical Arc Crater at 0.499 MW/cm <sup>2</sup> , Slightly Above Plasma Onset 3000x .....	56
4.14	Small Arcing Crater Near Plasma Onset BSE Conformation on the Right 5280x .....	57
4.15	Small Weakly Formed Crater Near Plasma Formation Power Density 6000x .....	58
4.16	Typical Unipolar Arc Crater 11,100x .....	59
4.17	Explosively Vaporized Crater at Plasma Onset Power Density: 0.41 MW/cm <sup>2</sup> 5470x .....	59
4.18	Explosive Vaporization of a Surface Imperfection 652x .....	60
4.19	Closeup of Vaporized Area 2,640x .....	60
4.20	ZnSe Window with Unipolar Arc Damage 500x .....	62
A.1	Laser Pulse Energy Content Versus Laser Power Supply High Voltage Level .....	73



## ACKNOWLEDGEMENTS

I wish to thank Mr. Robert Sanders for his technical assistance and advice on the CO<sub>2</sub> laser facility. I would also like to express my gratitude to Mr. Tom Kellog for his assistance and technical advice on the scanning electron microscope and target preparation.

To my friend and colleague Commander John Olson, I offer my thanks for his friendship and support during our entire thesis ordeal. I offer my thanks to his wife Jean and his family for putting up with me for many a meal hour.

Lastly I wish to thank my wife Gail and son Michael for tolerating my long absences with a smile and being there when I needed them.

## I. INTRODUCTION

Study of the interaction of a high power laser with optically opaque material and subsequent damage is a topic of continuing research. Because of the applications to arc breakdown in a vacuum, fusion power and the strategic defense initiative (SDI) much of the research has centered on the laser created plasma and the resulting damage mechanism. A thorough understanding of the damage mechanism may lead to ways to prevent plasma arcing in accelerators and fusion reactors and to ways to enhance damage mechanisms for defense applications.

Previous research at the Naval Postgraduate School (NPS) on plasma-surface interaction effects using a neodymium-glass laser (wavelength of 1.06 microns) have included a wide variety of subjects and materials. Brooks [Ref. 1] investigated the plasma formation and asymmetries associated with induced electric and magnetic fields. Case [Ref. 2] investigated self generated magnetic fields in laser produced plasmas. Polk [Ref. 3] studied the desorption of gases from AISI stainless steel (SS) 304 surfaces. Hwang and Travers [Ref. 4,5] studied evaporation from SS 304 surfaces. Keville and Lautrup [Ref. 6] analyzed the unipolar arcing damage mechanism with particular emphasis on Titanium Carbide (TiC) coated SS 304. By this point Schwirzke and Taylor had determined that, with a high powered laser, the primary surface damage mechanism was unipolar arcing and that arcing did not occur until plasma formation had been observed [Ref. 7] Subsequent research by Hoover, Ryan and Shedd, Beally and Ulrich, Metheny, Jenkins and Schmidt, and Stephenson [Ref. 8-13] has concentrated on the various aspects of the laser produced plasma-surface interaction and unipolar arcing. These experiments confirmed that unipolar arcing is the dominant damage mechanism. This is consistent with the Schwirzke-Taylor unipolar arcing model [Ref. 7].

This study examines the plasma surface interaction and unipolar arcing using a CO<sub>2</sub> laser (10.6 microns) and compares the results to a refined Schwirzke model noting the effect of a different wavelength laser. This experiment was conducted using a recently installed and activated CO<sub>2</sub> TEA pulsed laser with an optically focused beam and SS 304 targets. The targets were irradiated in a vacuum chamber (10<sup>-6</sup> Torr). The target surfaces were examined using optical metallography and an electron microscope.

The study was performed in conjunction with Olson [Ref. 14] who examined targets under the same conditions but used an unfocused beam .

The secondary purpose of this research was to establish the newly activated CO<sub>2</sub> laser as a viable student research tool and validate operating procedures for it. Appendix A is the recommended operating procedures and pertinent comments on the operation of the laser.

## II. BACKGROUND AND THEORY

### A. INTRODUCTION

There are several theoretical models for laser produced plasma-surface interaction. This chapter deals with the development of the refined Schwirzke model of unipolar arcing [Ref. 15: pp. 2-7] from the Robson-Thonemann model [Ref. 16: pp. 508-512]. An understanding of the basic processes involved in the plasma-surface interaction is essential to its understanding. These processes consist of desorption, thermal evaporation, ion sputtering, and unipolar arcing.

### B. DEFINITIONS

#### 1. Desorption

Desorption is the process by which the bond between a solid surface and adsorbed gas molecules ( $H_2$ ,  $H_2O$ ,  $O_2$ , etc.) is ruptured resulting in the removal of these gas molecules from the solid's surface [Ref. 3: pp. 12-22]. This can be accomplished by several means: thermal, photon induced, and electron and ion impact. These all work by raising the energy of the gas molecule enough to overcome the surface bond. For stainless steel this is on the order of 1.5 - 40 kcal/mole (0.06 - 1.6 eV/molecule) depending on the type of chemical bond, temperature of the gas and the surface [Ref. 3: pp. 12-13].

#### 2. Sputtering

Sputtering is defined as the bombardment of a surface with ions, neutrals, and/or electrons which leads to the removal of surface atoms by binary collisions. These collisions increase the energy of the surface atom enough to allow it to escape the surface. Because of the binary nature of the collision, there is no thermal heating of the surface [Ref. 17: pp. 1047-1049]. Desorption and sputtering differ in that desorption applies only to gases and light elements deposited on the surface and includes mechanisms other than binary collisions, while sputtering applies to any atom (gases as well as surface material) being removed from the surface by binary collision.

The amount of sputtering is measured by sputtering yield, the mean number of atoms displaced from the surface per incident bombarding particle. Because this process has small yields, very sensitive detection methods or large amounts of bombardment have to be used. For the energy ranges and materials associated with



nuclear fusion (this includes stainless steel and laser produced plasmas) sputtering yields have been experimentally determined for various ions and surface materials. For light ions below a given energy threshold ( $E_{th}$ ) no sputtering occurs. As seen in equation 2.1, this threshold energy is strongly dependent on the mass of the incident particle and the target atom [Ref. 17: p. 1049].

$$E_{th} = \{1/(\gamma (\gamma -1))\} U_0 \quad (\text{eqn 2.1})$$

where

$\gamma = 4M_1 \times M_2 / (M_1 + M_2)^2$  is defined as the energy transfer factor

$$M_1 < M_2$$

$M_1$  is the mass of the incident atom

$M_2$  is the mass of the target atom

and  $U_0$  = surface binding energy.

Figure 2.1 (from [Ref. 17: p. 1049] ) shows the sputtering yield as a function of the incident energy. Using equation 2.1, the  $E_{th}$  for SS 304 for an incident hydrogen ion is calculated to be 68 ev.

The sputtered material consists mostly of neutrals with a wide range of energies and angular dependencies assumed to be approximated by a cosine distribution [Ref. 17: p. 1050]. Neutrals play a significant role in the unipolar arcing model which will be explained later in the chapter.

### 3. Thermal Evaporation

Thermal evaporation occurs when the surface of the material has been heated above its vaporization point. Thermal evaporation effects are normally observed only near focal spot craters which have been created by high power densities. Although this study is concerned with a focussed beam, it is principally concerned with the onset of unipolar arcing and plasma formation at much lower power densities than expected for widespread thermal evaporation.

### 4. Energy Coupling

Energy coupling is the mechanism by which the laser energy is coupled into the surface of the material. It is a function of the target materials heat characteristics

(vaporization point, heat capacity etc.), reflectivity of the surface, and the shielding effect of the laser produced plasma once it is formed. Plasma forms within a few nanoseconds of the pulse incidence so its shielding effects can be significant for long pulse lengths. [Ref. 18: pp. 333-346]

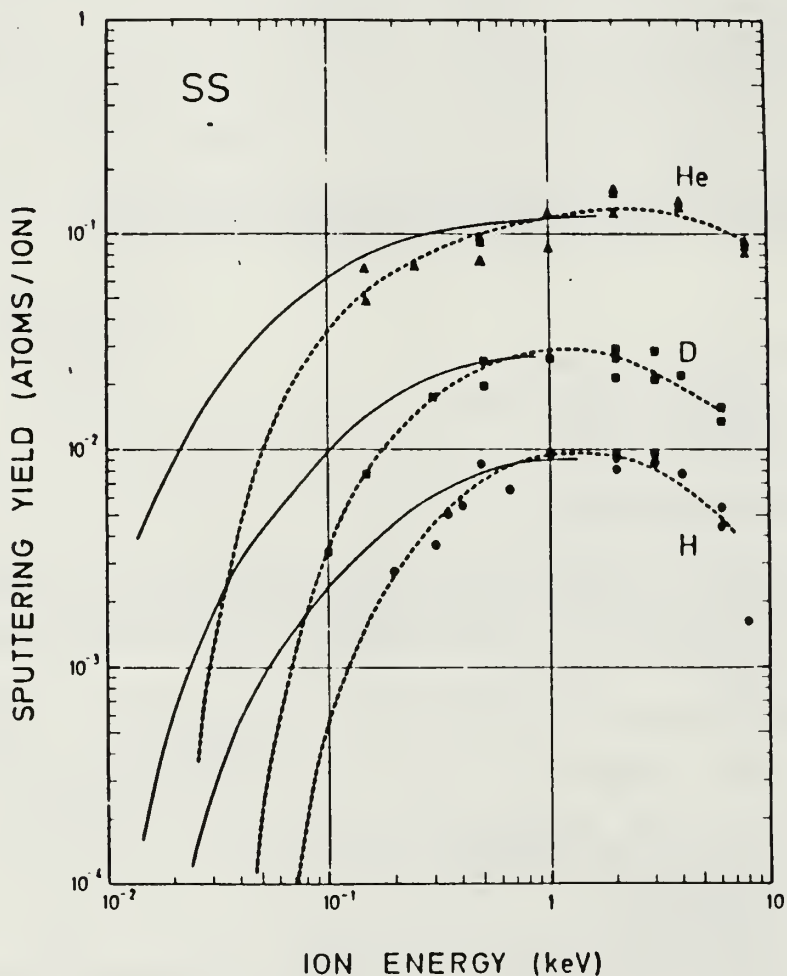


Figure 2.1 Sputtering Yield as a Function of Incident Energy for Stainless Steel and Various Incident Ions. Dashed Lines are for Single Energies Solid Lines are Averaged Energies Assuming a Maxwellian Distribution at Normal Incidence.

While the basic chemical properties of the material do not change, the reflectivity of the surface can vary greatly with changing temperature; for long pulse lengths, this can be significant. Figure 2.2 shows how the reflectivity of SS 304 changes as a function of time for 10.6 micron radiation on the order  $1.5 \times 10^8 \text{ W/cm}^2$ . This change in reflectivity can be attributed to the changes occurring on the surface of the material (desorption, melting, vaporization and unipolar arcing). The amount of energy that is absorbed by the surface is proportional to  $1 - R$ , where  $R$  is the reflectivity. This holds only if plasma is not formed. Once plasma is formed, both the surface and the plasma absorb energy. From Figure 2.2 it can be seen that energy coupling improves as the pulse progresses in time until it reaches a maximum at about 600 nanoseconds.

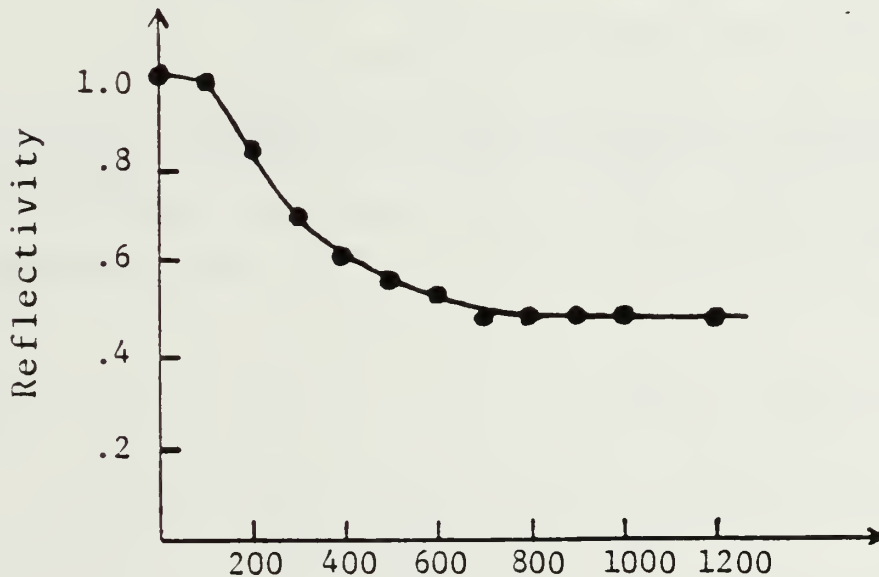


Figure 2.2 Reflectivity vs Time for 10.6 Micron Radiation for SS 304.

## 5. Plasma

A plasma is defined as a quasi-neutral gas of charged particles which exhibits collective behavior [Ref. 19: p. 3]. Quasi-neutrality implies that the electron density ( $n_e$ ) and the ion density ( $n_i$ ) are equal. Collective behavior means that any action on one particle or part of the plasma affects the rest of the plasma. One of the

consequences of this behavior is that a plasma has the ability to effectively shield itself from applied electric potentials. This shielding is accomplished over a finite distance called the Debye length which is defined by equation 2.2 (in MKS units) [Ref. 19: pp. 3-10]:

$$\lambda_D = (\epsilon_0 kT_e / ne^2)^{1/2} \quad (\text{eqn 2.2})$$

where

$\epsilon_0 = 8.854 \times 10^{-12} \text{ Nm}^2 / \text{C}^2$  is known as the permittivity of free space

$k = 1.38 \times 10^{-23} \text{ J/}^\circ\text{K}$  Boltzmann's constant

$n$  is the density of the plasma

and  $e = 1.6 \times 10^{-19} \text{ C}$  is the charge of an electron.

For a plasma with a given density there is a frequency at which the index of refraction goes to zero. When this occurs, all incident electromagnetic radiation is reflected from the plasma. This frequency is known as the plasma cutoff frequency. The characteristic frequency of oscillation of a plasma is defined by equation 2.3 [Ref. 19: p. 85]:

$$\omega_p = (ne^2 / \epsilon_0 m_e)^{1/2} \text{ rad/sec} \quad (\text{eqn 2.3})$$

where

$\omega_p$  is the plasma frequency

$n$  is the plasma density

and  $m_e = 9.11 \times 10^{-31} \text{ kg}$  is the mass of an electron.

This is equal to:

$$f_p = \omega_p / 2\pi. \quad (\text{eqn 2.4})$$



By substituting in the constants it follows that [Ref. 19: p. 85] :

$$f_p \sim 9n^{1/2} \quad (\text{eqn 2.5})$$

where  $n$  is in electrons/ $\text{m}^3$ .

The frequency of the  $\text{CO}_2$  laser is:

$$f = c/\lambda = 2.83 \times 10^{13} \text{ Hz} \quad (\text{eqn 2.6})$$

where

$c = 3.0 \times 10^8 \text{ m/sec}$  is the speed of light

and  $\lambda = 10.6 \times 10^{-6} \text{ m}$  is the wavelength of the laser.

In a plasma with no magnetic field the dispersion relationship is given by equation 2.7 [Ref. 19: p. 115]:

$$\omega^2 = \omega_p^2 + c^2 k^2 \quad (\text{eqn 2.7})$$

where  $k$  = the wave number.

As can be seen from equation 2.7 the cutoff frequency occurs when  $\omega = \omega_p$ . From equation 2.3 it can be seen that this occurs when

$$n_c = m_e \epsilon_0 \omega^2 / e^2. \quad (\text{eqn 2.8})$$

For a  $\text{CO}_2$  laser, this is found to be  $9.93 \times 10^{18} \text{ cm}^{-3}$ . It is important to note that refraction can still be significant at plasma densities as low as  $10^{16} \text{ cm}^{-3}$  [Ref. 19: pp. 116-125].

The plasma that is being created is in contact with the conducting surface of the target. Because of this, there exists a potential between the plasma and the target.

Due to the collective behavior of the plasma, the potential is shielded within a few Debye lengths of the surface. The area in which this occurs is known as the plasma sheath and the potential as the sheath potential. The sheath potential is also known as a floating potential, and can be described by equation 2.9:

$$V_f = (kT_e/2e)\ln(m_i/2\pi m_e) \quad (\text{eqn 2.9})$$

where

$k$  = Boltzmann's constant

$T_e$  = electron temperature

$e$  = electron charge

$m_i$  = ion mass

$m_e$  = electron mass.

It is easily seen that this floating potential is primarily dependent on the electron temperature. As the electron temperature increases  $V_f$  increases. [Ref. 20: p. 3].

### C. UNIPOLAR ARCING

Normally arcing is thought to require two electrodes, a cathode and an anode. Unipolar arcing is where arcing occurs with only one electrode and a surrounding plasma.

#### 1. Robson-Thonemann Model

The term unipolar arc was first used by Robson and Thonemann to describe the arcs observed on a metal surface in a plasma. They proposed that this arc was unipolar in that it initiated with only a single electrode and was sustained by a flow of electrons in the plasma. [Ref. 16: p. 508]

The sheath potential defined by equation 2.9 allows the plasma to maintain a positive potential with respect to the surface of the material. In order to maintain the quasi-neutrality of the plasma, as electrons flow from the plasma to the surface, an equal number of ions have to return to the surface. Figure 2.3 [Ref. 16: p. 509] illustrates this equilibrium flow of ions and electrons from the plasma to the surface. As the  $T_e$  increases, the  $V_f$  continues to increase until it reaches a point high enough to

initiate and sustain an arc. When arcing occurs, there is extensive electron emission from the cathode spot. As the electrons leave the surface (which is negative with respect to the plasma), the potential difference at the cathode spot decreases. This lowered potential is called the cathode fall potential ( $V_c$ ) of the arc. Since  $V_c$  is lower than  $V_p$ , more electrons can return to the surface. These electrons effectively close the current loop. Figure 2.4 depicts the flow of electrons and ions to the surface after arcing has initiated.

These conditions generate a circulating current ( $I_c$ ) which is defined by equation 2.10 as:

$$I_c = A n_e (kT_e / 2\pi m_e)^{1/2} \times \{ \exp(-V_c / kT_e) - \exp(-V_p / kT_e) \} \quad (\text{eqn 2.10})$$

where

$A$  = Surface area exposed to the plasma

and  $n_e$  = electron density in the plasma.

If  $I_a$  is defined as the minimum current density required to maintain an arc. Then  $I_c > I_a$  implies that the arcing process will continue until  $I_c < I_a$ . The magnitude of  $I_a$  is dependent on the composition of the surface material. The electron density is assumed to be constant and contributes to the return current over the entire area of the surface [Ref. 16: p. 508].

This model of a unipolar arc explains the basic arcing mechanism but neglects several important aspects of the process. It assumes a constant electron density but does not explain how the electrons from the cathode spot would distribute themselves to allow this and still have a return current of electrons to maintain the plasma quasi-neutrality. It also neglects the electric fields that are being generated and their interaction with the electron flow and the arcing process.

## 2. Schwirzke-Taylor Model.

The Schwirzke-Taylor unipolar arcing model takes the basic Robson-Thonemann model and extends it substantially. It explains the significance of the electric fields. It also addresses the distribution of the electrons and the role they play in the generation of the electric fields.

This model is explained in a series of reports that Schwirzke (et al) published in 1981, 83, and 84 [Ref. 7,15,20]. These reports were prepared based on analysis of SS 304 targets irradiated with a Korad K-1500 neodymium laser (1.06 microns). It explains the necessity of an uneven plasma density above the cathode spot, which creates a radial electric field ( $E_r$ ), thus creating a ring of reduced sheath potential and allowing a larger number of electrons to reach the surface and maintain the quasi-neutrality of the plasma. Schwirzke postulated this ring would form directly over the cathode spot due to the increasing plasma density caused by arcing. This increase in plasma density creates an electron pressure gradient, reduces the Debye shield length in this vicinity and allows enhanced arcing. Figure 2.5 shows the unipolar arcing model presented by Schwirzke and Taylor.

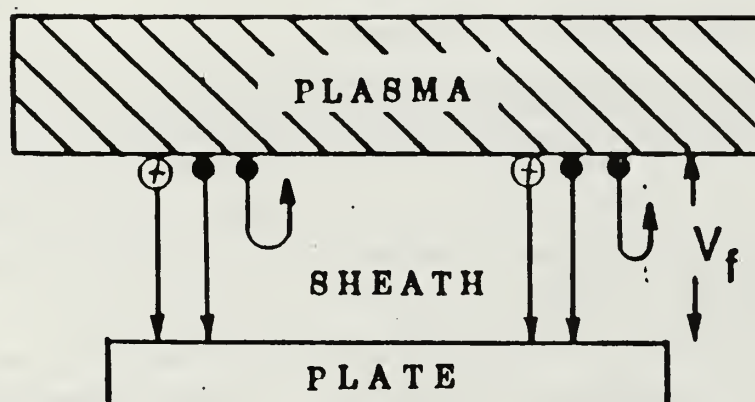


Figure 2.3 Electron - Ion Flow from Plasma to a Metal Surface  
Prior to Cathode Spot Formation.

*a. Sequential Unipolar Arc Model*

The unipolar arcing process is a complex series of interrelated processes that occur in a very short (nanoseconds) time period. It is most easily presented and comprehended when viewed as a series of sequential events. A model is proposed here which incorporates the details of the Schwirzke-Taylor model and presents them as a

Sequential Unipolar Arc model. It should be remembered that unipolar arcing occurs with the onset of plasma formation, and this has been observed (depending on the incident energy) within a few nanoseconds of the laser pulse incidence. These events (in order) consist of : onset of plasma formation, onset of electric field and floating potential buildup, electric field concentration, enhanced electron emission, whisker vaporization, self sustaining feedback mechanism, and arc cessation. Although the electric field concentration, enhanced electron emission and whisker vaporization are not necessary for arc formation, they allow the arcing process to occur at a lower electric field strength ( $10^7$  volts/cm with whiskers and a dirty surface vs.  $10^9$  volts/cm for a clean surface) [Ref. 21: p. 17].

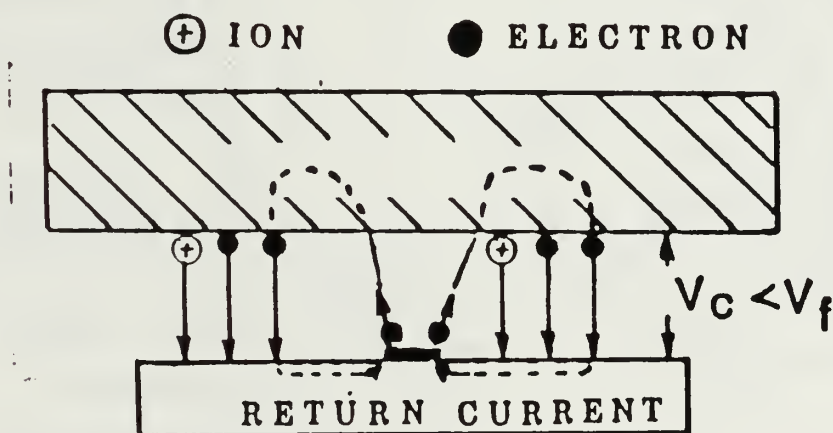


Figure 2.4 Electron - Ion Flow from a Plasma to a Metal Surface  
After Arcing has Initiated.

#### *b. Desorption*

When the laser pulse reaches the target surface, it is partially reflected. Some of the energy is lost to the surface where it heats the surface and causes the lighter surface contaminants to be desorbed. These contaminants consist primarily of gases ( $H_2$ ,  $N_2$ ,  $O_2$  etc.) and water vapor adsorbed when the surface is exposed to air.





$$E^2 = 4E_0^2 \sin^2(2\pi z / \lambda) \quad (\text{eqn 2.11})$$

where

$E_0$  = Electric field magnitude (E)

and  $z$  = distance from target surface.

Free electrons within the plasma will oscillate most rapidly at  $z = 1/4 \lambda$  from the surface. Because of this rapid oscillation and the close proximity to neutrals being desorbed from the surface, it is most plausible that the plasma will begin to form at this distance [Ref. 20: p. 16].

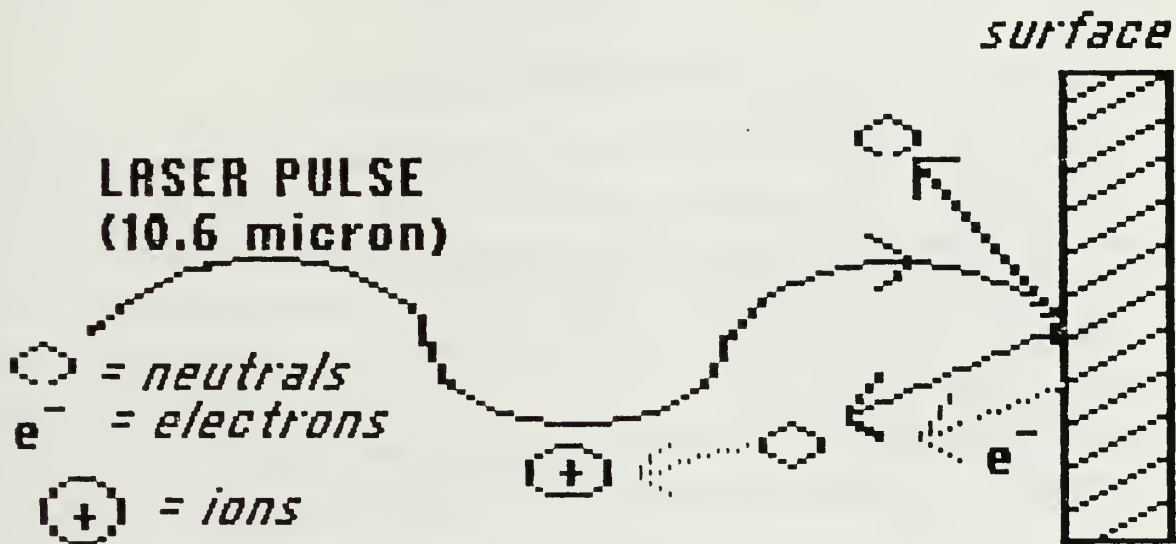


Figure 2.6 Onset of Plasma Formation.

### c. Electric Field Formation

Electrons have much lower mass and consequently higher thermal velocities than the ions. The ions, due to their greater mass, have greater resistance to movement. This leads directly to an ion rich boundary layer between the plasma and the surface. The plasma is positive with respect to the target surface. This potential difference is the floating potential  $V_f$  and an electric field begins to form normal to the surface (see Figure 2.7). As high energy electrons reach the target surface an equal number of ions reaches the surface (see Figure 2.3). This is required to maintain the

plasma's quasi-neutrality. This quasi-neutrality relationship can be defined by examining the current flow and is given by equation 2.12:

$$J = J_e + J_i = q_e n_e v_e + q_i n_i v_i = 0 \quad (\text{eqn 2.12})$$

where

$J$  = current density

$q$  = particle charge

$n$  = particle density

$v$  = fluid velocity

and the subscripts  $e$  and  $i$  refer to electrons and ions respectively.

As long as the plasma density is less than the critical density ( $n_c$ , given by equation 2.8) laser energy is still reaching the surface of the target. This energy continues the desorption process. The electrons and ions reaching the surface recombine on the surface causing additional heating. At this point the  $E$  field is still normal to the surface within the plasma. By symmetry arguments, there is no reason for there to be a higher concentration of electrons at one spot than at another. As the electrons and ions increase the plasma density, the Debye length decreases. Equation 2.13 gives the relationship for the  $E$  field in the plasma sheath. From this it can be seen that as  $\lambda_D$  decreases,  $E_s$  increases.

$$E_s \sim V_f / \lambda_D. \quad (\text{eqn 2.13})$$

#### ***d. Plasma Density Buildup***

The plasma density continues to increase until it approaches  $n_c$ . The amount of laser energy reaching the surface decreases and the amount being absorbed by the plasma increases. As energy is absorbed by the plasma the electron temperature ( $T_e$ ) continues to rise resulting in an increase in  $V_f$ . This increase in  $V_f$  causes increased ion acceleration in the sheath. Ions move toward the negative surface of the target and hit the surface with more energy. Equal numbers of ions and electrons still continue to reach the surface (high energy electrons) and recombine, continuing the

heating process. The higher energy ions reaching the surface cause sputtering of neutrals, providing more neutrals to be ionized and thus continuing to increase the plasma density.

Eventually  $n$  reaches  $n_c$  and cutoff occurs. The laser energy is now being partially reflected and partially absorbed by the plasma with no direct laser energy reaching the surface.  $T_e$  increases to a point where the inelastic collisions and the ionization process remove energy at a rate equal to the amount being absorbed from the laser. Thus  $kT_e$  increases to a point and then remains essentially constant.

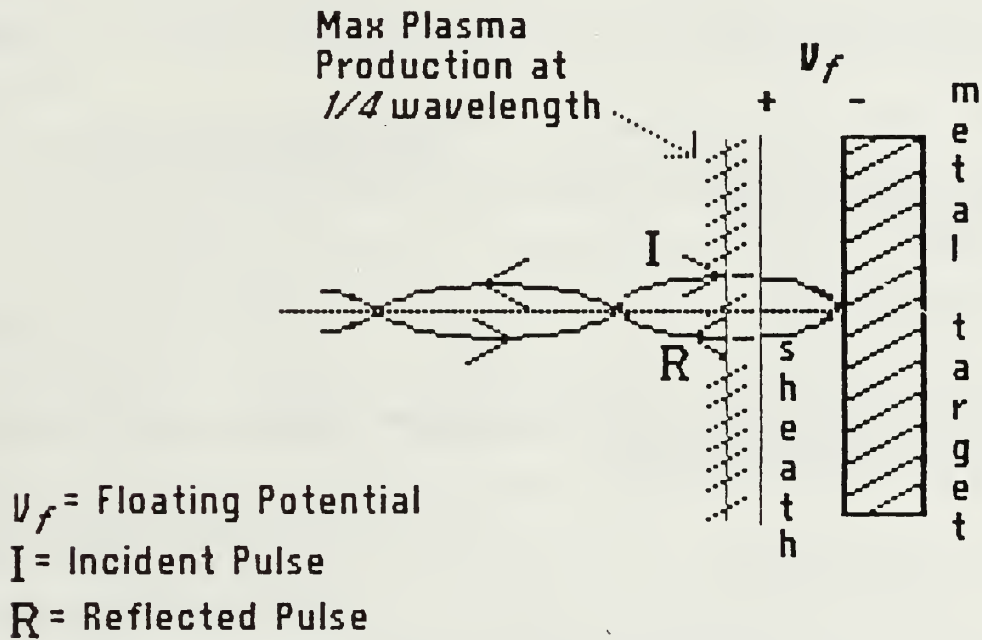


Figure 2.7 Electric Field and Floating Potential Formation.

As the plasma density and  $T_e$  increase, the magnitude of the  $E$  fields in the plasma and in the sheath (given by equation 2.13) continue to increase. The electric field within the plasma is created by the pressure gradient of the electrons ( $\nabla P_e$ ). The field can be determined by considering the electrons as a "fluid" and examining the equation of motion for this fluid. Equation 2.14 gives this relationship.

$$\rho_e \frac{\partial V_e}{\partial t} = -en_e(E + V_e \times B) - \nabla P_e + n_e e / \sigma j = 0 \quad (\text{eqn 2.14})$$

where

$\rho_e = n_e m_e$  is the electron mass density

$V_e$  = fluid velocity of the electrons

$P_e$  = electron pressure

$j$  = current density

$\sigma$  = electrical conductivity.

By setting  $B = 0$  and noting that the electron inertial term is insignificant for the time period of arc evolution, this becomes:

$$E = j / \sigma - \nabla P_e / n_e e. \quad (\text{eqn 2.15})$$

For a weakly ionized plasma the  $j / \sigma$  term is independent of  $n_e$  and small in comparison to  $E_0$  so the second term in equation 2.15 dominates, and the electric field in the plasma becomes:

$$|E| = \nabla P_e / n_e e. \quad (\text{eqn 2.16})$$

Since  $\nabla P_e$  is equivalent to  $kT_e \nabla n$  for isothermal compression ( [Ref. 19: p. 67] ), this ambipolar electric field becomes:

$$|E| = (kT_e) (\nabla n / n) . \quad (\text{eqn 2.17})$$

Since  $\nabla n / n = 1 / d$  where  $d$  is the characteristic pressure gradient length. For the case of the maximum plasma heating at a distance of  $\lambda/4$  from the surface, the gradient length will be  $d = \lambda/4$ .

To compare this ambipolar  $E$  with  $E_s$ , we can estimate  $kT_e$  for a weakly ionized plasma as  $kT_e \sim 10\text{ev}$  [Ref. 22: p. 40]. When these values are substituted into equation 2.17, the magnitude of the electric field normal to the surface, in the plasma, is  $E = 3.77 \times 10^6$  V/m. To find  $E_s$ , for a weakly ionized plasma,  $n_e \sim 10^{14} \text{ cm}^{-3}$ , substituting these values into equation 2.2 for  $\lambda_D$ , and equation 2.9 for  $V_p$  and then substituting the resultant values into equation 2.13 to find the  $E$  field in the sheath,  $E_s = 1.92 \times 10^7$  V/m. Therefore it is clear that  $E_s > E$ . Note that the ambipolar  $E$  is not



affected by a change in  $n_e$ , but as  $n_e$  is increased,  $E_s$  increases. Therefore at  $n_e = n_c = 10^{19} \text{ cm}^{-3}$  we have  $E_s \gg E$ .

The plasma density buildup occurs concurrent with the start of the arcing processes explained below. When arcing starts: more surface material is ejected into the plasma, which increases the plasma density, which increases the E field, and in turn increases the number of electrons and ions being driven to the surface. Sputtering increases and the recombination energy heats the surface enough to allow evaporation of the metal atoms. The increased E field continues to drive the arc. Thus there is a self sustaining feedback mechanism once the arcing is initiated. This feedback mechanism also exists to a lesser extent, prior to arc initiation, in the form of increased sputtering and possible evaporation of metal ions from the surface due to the higher energy ions bombarding the surface and the recombination energy being deposited in the surface.

#### *e. Electric Field Concentration*

For a perfectly smooth, clean surface the electric field "lines" would be evenly spaced throughout the plasma. As previously mentioned, the E field required for field emission from a clean surface is  $10^9 \text{ V/m}$ . For a dirty surface the E field required is much less,  $10^7 \text{ V/m}$ . This phenomenon can be explained by dirt and small surface imperfections causing a concentration of the E field. One type of surface imperfection is called a whisker. Whiskers are typically on the order of  $10^{-4} \text{ cm}$  in height with a base radius less than  $10^{-5} \text{ cm}$  and a tip radius much smaller than the base radius (see Figure 2.8) [Ref. 23: pp. 32-38].

This localized enhancement of the E field effectively focusses the ion bombardment onto the whisker tip. In turn this causes increased sputtering, heating and vaporization. The increase in the neutral particles immediately above the whisker tip allows for increased ionization and subsequently increased plasma density in the vicinity of the whisker. Since  $\lambda_D$  varies inversely with the plasma density,  $\lambda_D$  decreases and results in a higher  $E_s$  at the whisker. This increase in the plasma density is rapid and results in an equally rapid rise in  $E_s$ .

#### *f. Enhanced Electron Emission / Arc Initiation*

Arcing is initiated by the emission of electrons from the surface of the material by the aforementioned processes. Parker states that "the emission of electrons from a conducting surface is highly dependent on the magnitude of the field and the temperature of the surface" [Ref. 23: p. 17]. The applied electric field lowers the

potential barrier of the surface of the conductor. Field emission of electrons is described as the quantum-mechanical tunneling of electrons through this lowered potential barrier. As previously stated, the threshold for electron emission from a clean, smooth surface is  $10^9$  V/m.

The enhancement due to the change in the geometry of the E field at the whisker tip is given by equation 2.18:

$$b = h / r_t \quad (\text{eqn 2.18})$$

where

$b$  = enhancement factor

$h$  = whisker height

$r_t$  = radius of the whisker at the tip.

And

$$E_{\text{enhanced}} = bE. \quad (\text{eqn 2.19})$$

$b$  can vary from 10 to 1000 depending on the whisker [Ref. 24: p. 49].

The previously calculated  $E_s$  for a weakly ionized plasma was  $E_s = 1.92 \times 10^7$  V/m. This then requires an enhancement factor of 100 to reach field emission ( $10^9$ , V/m), which is well within the range of  $b$  as mentioned above.

#### *g. Whisker Vaporization*

Due to the extremely short time frame over which the E fields increase, the enhanced electron emission from a whisker can be characterized as explosive. It is accompanied by light emission and gas desorption characteristic of an expanding plasma [Ref. 24: p. 49].

If there is field emission from a whisker and current flow through the whisker, then the voltage drop along a whisker is given by:

$$V = Ri \quad (\text{eqn 2.20})$$

where

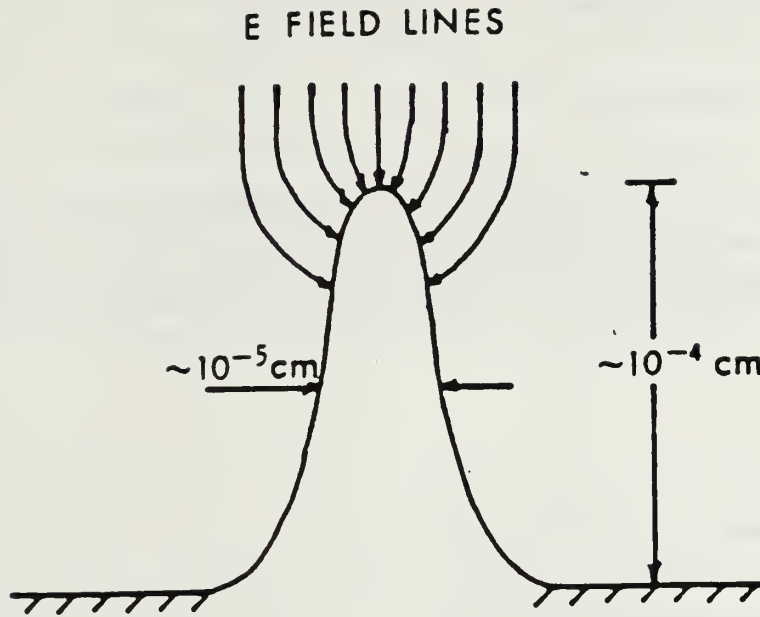


Figure 2.8 Local Electric Field Enhancement at Whisker Tip.

$V$  = voltage drop

$R$  = resistance

and  $i$  = current.

Resistance is defined as:

$$R = \rho \ell / A \quad (\text{eqn 2.21})$$

where

$\rho$  = resistivity

$\ell$  = whisker length in cm

and  $A$  = whisker cross sectional area.

Current is given by:

$$i = jA \quad (\text{eqn 2.22})$$

where  $j$  = current density. Equations 2.20 through 2.22 can be combined to yield the relationship for the electric field in the whisker as:

$$E_w = V / \ell = \rho j. \quad (\text{eqn 2.23})$$

If  $j$  is set equal to  $j_{EFE}$  the observed current density for enhanced field emission ( $10^7$  amperes /  $\text{cm}^2$ ) and  $\rho$  for SS 304 at  $75^\circ \text{ F}$  is used, then  $E$  is determined to be 7140 V/m. The power available for vaporization is (assuming enhanced field emission i.e. arcing):

$$P_v = j_{EFE} E. \quad (\text{eqn 2.24})$$

Which yields  $P_v = 714 \text{ Mwatts/cm}^3$ .

If a whisker is assumed to be a right circular cylinder with a height of 1 micron, and a radius of 0.05 microns, its volume is  $7.845 \times 10^{-15} \text{ cm}^3$ . Using the density of SS 304 as  $8.0 \text{ g/sm}^3$  and a latent heat of vaporization of  $340.4 \text{ kJ/mole}$ , it requires  $1.192 \times 10^{-13} \text{ J}$  to vaporize a whisker. Using the pulse length for the Lumonics  $\text{CO}_2$  laser of  $4.55 \text{ } \mu\text{sec}$  and the volume of the whisker, this translates to  $3.33 \text{ Mwatts/cm}^3$ . Assuming a 95% reflectance (from Figure 2.2) for the surface, there is still  $35.7 \text{ Mwatts/cm}^3$  available to vaporize the whisker. Since there is more than adequate energy available, the whisker vaporizes in a manner mentioned earlier as "explosive".

The electric field required to drive the arc can be approximated by:

$$|E_{\text{arc}}| \sim V_c / \lambda_D \leq V_f / \lambda_D. \quad (\text{eqn 2.25})$$

Where  $V_c$  is the cathode fall potential discussed previously with the Robson-Thonemann model. It is easily seen that the plasma density continues to increase (more neutrals being ejected into the plasma and being ionized) and  $\lambda_D$  continues to decrease. This causes  $E_{\text{arc}}$  to increase and provides a self-sustaining feedback to drive the arc.

The mean free path of electrons is greater than the sheath width. This allows for increased ionization of neutrals in the immediate vicinity of the arc. These conditions lead to a local potential drop ( $\Delta V$ ). These events cause an increase in the

plasma pressure above the cathode spot which results in the creation of a radial E field ( $E_r$ ). This field points outward from the plasma above the cathode spot (see Figure 2.5). The increase in  $\Delta V$ , due to the pressure build up over the cathode spot, is not with respect to  $V_f$  in Figure 2.5, rather the dense plasma is biased via  $V_c < V_f$  pulling the curve down as schematically indicated in the figure. This leads to a ring of lowered potential with  $V_r < V_f$  which allows an increased electron return current. This current closes the unipolar arc current loop. The combined effects of  $E_{arc}$  and  $E_r$  produce a self-sustaining feedback mechanism that continues to drive the arc until arc cessation. These events are best represented by Figure 2.5 which illustrates the refined Schwirzke model [Ref. 15: p. 5].

#### *h. Arc Cessation*

As arcing continues, craters are created as more and more surface material is ejected into the plasma from the cathode spot. As the  $\lambda_D$  decreases with the increased plasma density, the plasma conforms to the contour of the crater. As the crater gets deeper, the dense plasma in the crater reduces the electron heat flux from the laser heated plasma. This causes a decrease in the electron temperature ( $T_{elocal}$ ) in the localized region in the crater and above the cathode spot. Since the potential difference,  $V_c$ , is dependent on the electron temperature, the  $V_c$  and thus the  $E_{arc}$  decrease with  $T_{elocal}$ . This continues until  $E_{arc}$  can no longer sustain arcing.

#### *i. Discussion of Model Assumptions*

This model assumes normal incidence for the laser radiation. This is done to make it easier to understand where the maximum field intensity and thus when plasma formation is going to occur. It should be noted that normal incidence is not a requirement for this model to work. The basic arcing damage mechanism is dependent on  $E_s$ , i.e. on the distance the plasma forms from the material surface, which is dependent on  $\lambda_D$ . This model does not take into account the skin depth of the laser radiation interacting with the conductor. This does not affect the basic sequence of events but it might affect the magnitude of  $E_{arc}$  (skin depth is proportional to the wavelength of the incidence radiation) for arc initiation and arc cessation.

This model is limited in that it addresses only one arc where in reality the arcing density can range from one for an entire surface to 800,000 /cm<sup>2</sup>. However, it can be seen that once the basic mechanism is understood, expanding it to multiple arcs is quite simple.



The model also implies that  $E_{\text{arc}}$  can be predicted. This would be true if all of the values were known. However, the exact values for the onset of unipolar arcing are not known for most materials. With this in mind the experiment described in the next chapters undertakes to determine the value of laser energy required for arcing onset for a 10.6 micron  $\text{CO}_2$  laser.

### III. EXPERIMENTAL METHOD

#### A. INTRODUCTION

This experiment was designed to determine the amount of power required for onset of unipolar arcing for SS 304 in a vacuum with a CO<sub>2</sub> laser. This required a variety of equipment which is described in the following sections. The SS 304 targets were irradiated with a high power pulsed CO<sub>2</sub> laser in a 10<sup>-6</sup> Torr vacuum. The laser energy was routed into the vacuum chamber via a beam splitter and mirrors, and then through a NaCl window. After the targets were irradiated, they were examined with an optical microscope and a scanning electron microscope. Figure 3.1 depicts the experimental setup.

#### B. EXPERIMENTAL APPARATUS

##### 1. Laser

A Lumonics TE 822 HP high energy TEA pulsed laser was used as the laser source. It is capable of producing 20 joules of output and has an adjustable pulse width from 0.05  $\mu$ sec to 5.0  $\mu$ sec. This, along with the similar experiment conducted by Olson [Ref. 14] was the first use of this laser facility at NPS. This necessitated learning how to use the laser and conducting operational tests before commencing any research. This laser uses an optically active medium of carbon dioxide, nitrogen, and helium, which is excited by a transverse electrical discharge. A population inversion results from the discharge electrons colliding with the CO<sub>2</sub> and N<sub>2</sub> molecules. Since one of the N<sub>2</sub> molecular upper vibrational levels possesses an excitation energy which is approximately equal to that of the CO<sub>2</sub> molecule, the N<sub>2</sub> serves to enhance the magnitude of the population inversion by the efficient transfer of vibrational energy during collisions between the CO<sub>2</sub> and N<sub>2</sub> molecules. Thus, the N<sub>2</sub> serves as reservoir of energy which directly influences laser peak power and pulse length. [Ref. 25]

Helium is used to obtain a well diffused electrical discharge. The He also removes heat (generated by the electrical discharge) and lowers the gas mixture temperature. This results in less depletion of the CO<sub>2</sub> upper vibrational level, and the interaction of the CO<sub>2</sub> and He increases relaxation of the CO<sub>2</sub> lower vibrational level. Therefore, the use of He allows the laser to be pumped at higher discharge currents, which produces a larger population inversion and thus higher power. The high voltage

power supply and gases were cooled by a Flowrite (RPCX mod 387) chill water unit with a flow rate of 25 gallons per hour at  $20 \pm 5^{\circ}\text{C}$ .

The Lumonics laser with a multimode optic emits a 30 x 33 mm beam of approximately rectangular shape. The pulse shape can be varied in time from 0.05  $\mu\text{sec}$  to 5.0  $\mu\text{sec}$  by adjusting the gas mixtures. For a variety of reasons, a standard long pulse mixture, resulting in a 4.55  $\mu\text{sec}$  pulse was used (see Figure 3.2). The standard gas settings for long pulse are: 10 psig on the pressure gauges for  $\text{CO}_2$ ,  $\text{N}_2$ , and He, 8 standard cubic feet per hour (SCFH) for  $\text{CO}_2$  and  $\text{N}_2$ , and 6 SCFH for He. This provided a reasonable pulse shape with a good distribution of the laser energy in time. The power density was varied by adjusting the voltage of the capacitor discharge and the use of NaCl windows to reduce the amount of power transmitted into the vacuum chamber. Although NaCl has excellent transmittance at 10.6  $\mu\text{m}$ , by tilting the the window slightly from normal incidence, from 5-11 % of the laser energy was reflected from the front and back surfaces of the window.

The laser operating procedures provided by the laser technical manual [Ref. 26], were clear but poorly organized, with important safety considerations spread throughout the manual. To provide future operators with a consolidated set of operating guidelines, operating procedures and safety considerations were rewritten with procedures required for operating the facility at NPS. These procedures are provided as Appendix A.

## **2. Vacuum Chamber**

The vacuum system used in this experiment was originally a vacuum electroplating system. It has been substantially modified and refitted with a four port vacuum chamber in place of the electroplating equipment. It was manufactured by Veeco Vacuum Systems and modified by NPS personnel. It utilizes a mechanical pump and a diffusion pump with a liquid  $\text{N}_2$  coolant system, to achieve a vacuum of approximately  $10^{-6}$  Torr in the chamber. The ionization gauge was not located directly off of the chamber. It was located at the top of the diffusion pump, making it difficult to get exact readings of the vacuum in the chamber. A target wheel, with spots for six targets, was mounted through one of the ports to allow easy target alignment and irradiation of more than one target without having to break the vacuum. Two of the other ports were sealed with plexiglass windows to absorb any reflected laser energy and allow viewing into the chamber. The laser beam was brought into the chamber through a 3" NaCl window. This window had to be polished and calibrated to determine the transmittance, before each laser session.

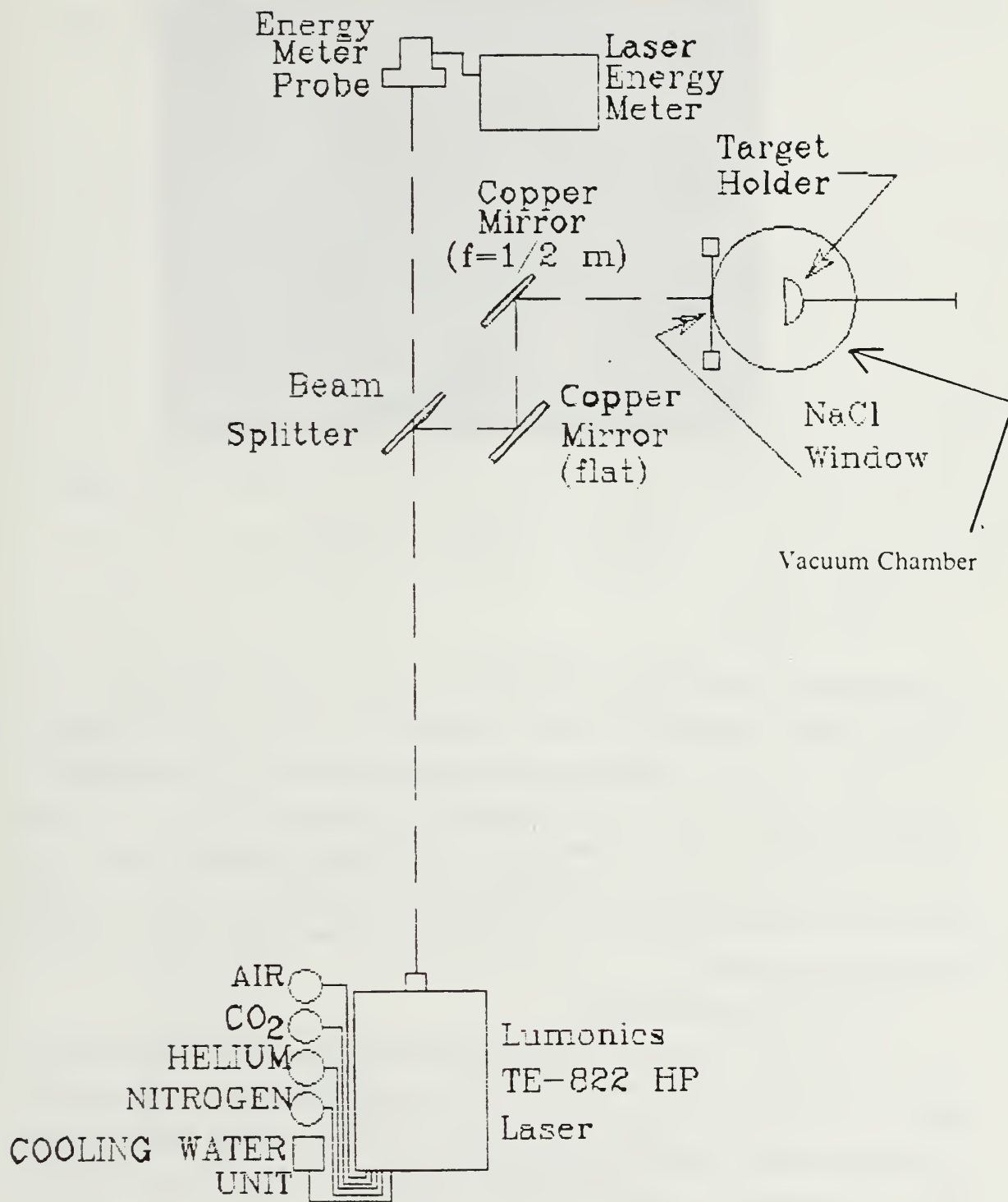


Figure 3.1 Experimental Arrangement.

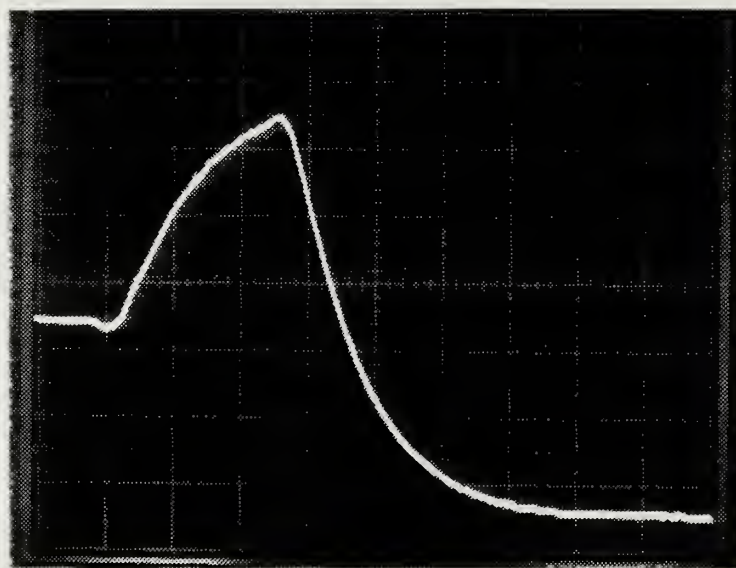


Figure 3.2 4.55 $\mu$ sec FWHM Pulse Width for Standard Long Pulse Gas Settings  
Horizontal Axis - 2  $\mu$ sec per division  
Vertical Axis 0.1 Volts per Division.

### 3. NaCl Windows

NaCl has excellent transmittance and low absorption at 10.6  $\mu$ m. Unfortunately it is extremely hygroscopic. After only 3 to 4 hours of exposure to the relatively humid environment in the lab facility, the NaCl window had absorbed enough moisture to turn cloudy and require polishing. This was a time consuming and inconvenient process. Two ZnSe 3" windows were purchased when the facility was originally proposed. These windows should have withstood the energy output of the laser but did not. During initial experimentation, the coating on one of the ZnSe windows was severely damaged by a relatively low power pulse. This necessitated using the NaCl windows.

### 4. Pyroelectric Energy Meters

The energy of the laser beam was determined by use of a pyroelectric energy meter. A pyroelectric energy meter measures the total incident energy on the probe. Power was calculated by using the pulse width and shape to calculate power from the total energy incident. Two different meters were used in the initial stages to provide a basis for comparison. A Laser Precision Corporation Rj-7100 Wide Band Energy Radiometer with a RjP-736 probe, and a Laser Precision Corporation Rk-3232



Pyroelectric Energy Meter with RkP-336 detector probe were used. Both instruments were in calibration and provided system accuracies of  $\pm 5\%$ . Both detector probes were designed to measure energy levels from 20 mJ to 10 J with favorable response in the 10.6  $\mu\text{m}$  wavelength with durations of 1 nanosecond to 1 millisecond.

### 5. Infrared Detector

To provide an accurate pulse width and shape, an Infrared Associates, Inc. HgCdTe Infrared Detector (Mod HCT-55) was utilized. This detector was very sensitive in intensity required for detection and in time to respond to an incident signal. Due to the sensitivity of the detector, it could not be used with direct incidence of the laser beam. Instead, the beam was reflected off plexiglass into the detector. To achieve these sensitivities, the detector had to be cooled with liquid  $\text{N}_2$ . To avoid damage to the electronics in the amplifier, the detector could not be connected to the amplifier until it was cooled to liquid  $\text{N}_2$  temperatures. The output from the amplifier was connected to an Hewlett Packard Model 468 Digital Storage Oscilloscope for analysis and photographic recording. Figure 3.2 is the pulse shape and width for the standard long pulse gas mixture. Analysis of it provides a Full Width Half Maximum (FWHM) pulse duration of 4.55  $\mu\text{sec}$ . This pulse shape was very consistent over the energy and power settings used.

### 6. Optics

Ordinary visible spectrum optics are not usable for the 10.6  $\mu\text{m}$  wavelength. They either absorb too much energy or are non-reflective or transmissive at this wavelength. This required the use of specialized optics.

The optical equipment provided for use with the  $\text{CO}_2$  laser consisted of:

1. One 3" diameter ZnSe beam splitter, 99.38% reflective, 0.13% transmittance, and 0.49% absorption at 45° incidence.
2. Two ZnSe 3" diameter windows with anti-reflective coatings, for use with the vacuum chamber.
3. One 3" diameter, 300 mm focal length (F.L.) convex copper mirror for beam expansion.
4. One 3" diameter 0.5 m F.L. concave mirror.
5. One 5" diameter 1.0 m F.L. concave copper mirror.
6. One 4" flat mirror (infinite F.L.).
7. Three 3" diameter NaCl windows (obtained later).
8. One 2" diameter NaCl window (obtained later).

The copper mirrors were assumed to have a worst case reflectance of 98.5% [Ref. 27: p. 44]. The NaCl windows absorb very little energy but, depending on the angle of incidence and the polished surface finish, have a reflectance of 5-11% from the front and back surfaces combined.

The high reflectance of the beam splitter allowed the energy meter to be operated below damage threshold of 1 MW/cm<sup>2</sup> for the probes. Unfortunately, this necessitated using the lowest scale on the meter with values on the low end of this scale. This resulted in a larger degree of uncertainty in the readings ( $\pm 5\%$ ).

#### **7. Scanning Electron Microscope.**

To view the damage done to the surface with any detail at the micron scale, required the use of an electron microscope with its shorter wavelength and attendant higher resolution. The Cambridge Stereoscan 200 Scanning Electron Microscope (SEM) was the primary means of target analysis. It provided magnifications from 30x to 300,000x with excellent resolution for micron size craters and surface features.

### **C. LASER FACILITY**

Prior to starting experimentation, the CO<sub>2</sub> laser facility had to be operationally tested and several parameters determined. The pulse width and shape for the standard long pulse gas settings were determined by using the infrared detector described earlier. It was determined that the pulse width and shape remained constant as a function of the gas mixture. It was also determined that the energy content of the beam remained constant as a function of gas mixture and high voltage discharge setting. Tables 1 through 5 provide the results of this pulse to pulse energy repeatability of the beam. The beam energy varied from  $\pm 1.26\%$  to 1.94% (depending on the gas mixture).

In order to determine the approximate high voltage discharge KV settings for the desired energy range, a study was made to determine KV setting vs. energy content of the beam for the standard long pulse gas settings. The results of this study are provided in graphical form in Appendix A as Figure A.1.

During the course of the experimentation, it was discovered that the optical alignment of the laser and thus the laser pulse shape was sensitive to temperature changes of  $\pm 10^\circ\text{F}$  or more. The change in the beam shape had the effect of significantly changing the energy distribution in the beam. Which resulted in having to estimate the energy in the hot spots for shots 1 through 10 (see the section in Chapter IV on beam inaccuracies). The optics were originally aligned with the lab facility at

approximately 55°F. When the building heat was turned on and the vacuum chamber was in operation, the ambient temperature ranged from 65°F to 85°F.

## D. PROCEDURES

### 1. Target Preparation

SS 304 targets were machined from 0.5 inch diameter rod stock to a thickness between 0.125 and 0.25 inches. Each target was then mounted in bakelite holders to facilitate mechanical polishing. The surface was then sanded with progressively finer sandpaper until the finish was smooth enough to polish on polishing wheels with 600 micron  $\text{Al}_2\text{O}_3$  slurry. The targets were then polished in three stages with progressively finer grits. A 600 micron grit, a 1 micron grit, and a 0.25 micron grit slurries were used. This method of surface preparation produced a smooth mirror like finish on the target face. The targets were then cleaned with de-ionized water and stored in a desiccant chamber until needed. When needed the targets were broken out of the bakelite holder, cleaned with de-ionized water, acetone, and ethanol and then blown dry with  $\text{N}_2$  (this procedure required approximately 1.5 hours to polish). Once polished, the targets were handled with disposable plastic gloves and tweezers to avoid deposition of fingerprint oils and dirt on the surface.

Irradiated targets were immediately mounted on stubs with a colloidal suspension of silver to allow for good electrical conductivity in the SEM. SEM analysis was scheduled as closely as possible with irradiation. To avoid contamination of the vacuum in the SEM, a minimum of 8 hours drying time was required for the silver paint. While awaiting examination, the targets were stored in a desiccant chamber to reduce oxidation and contamination. After cleaning, 5 targets were placed on the target wheel, leaving one space blank to facilitate alignment.

To facilitate examination of the thermal effects observed on high power density targets, several targets were cut in cross section at a 45 degree angle. This was accomplished using an Isomet 11-1180 Low Speed Saw and a brass blade with an embedded diamond cutting edge. The targets were then examined in the SEM, then chemically etched using Kalling's Reagent number 2. A solution of 100 ml HCl, 100 ml Ethanol, and 5 g.  $\text{CuCl}_2$ . This allowed examination of the grain structure of the material.

## 2. Target Alignment

Target alignment was accomplished by using a low power HeNe laser with a small beam width to perform a rough alignment. Once the rough alignment was completed, a 10x beam expander was used to expand the beam to approximately the same size as the CO<sub>2</sub> laser beam. This facilitated alignment of the optics and spot size adjustments.

## 3. Power Density

For this experiment, the spot size was maintained at approximately one cm<sup>2</sup> and the power density was adjusted by raising or lowering the high voltage discharge, and the placing of additional NaCl windows in the beam path.

The power density was calculated from the spot size and the energy meter reading by equation 3.1:

$$P_d = ER_b R_m T_w / T_b A t \quad (\text{eqn 3.1})$$

where

$P_d$  = power density at the target surface in W/cm<sup>2</sup>

$E$  = energy meter reading in joules

$R_b$  = beam splitter reflectance = 0.9938

$R_m$  = copper mirror reflectance = 0.985

$T_w$  = transmittance of NaCl window

$T_b$  = beam splitter transmittance

$A$  = spot size

and  $t$  = FWHM pulse duration.

It was not possible to make the spot size smaller than 1 cm<sup>2</sup> and still achieve power densities low enough to find the threshold of plasma formation, additionally, at spot sizes smaller than 1 cm<sup>2</sup> there was severe astigmatism in the reduced spot, which resulted in enhanced hot spots in the beam area.



#### 4. Determination of Plasma Onset

Once mounted on the target wheel, the targets were placed in the vacuum chamber, the chamber sealed and evacuated to  $10^{-6}$  Torr (this required approximately 45 minutes). After the vacuum was achieved the target alignment was reverified, and beam energy adjusted. The energy was adjusted by placing a plexiglass stopper before the vacuum chamber and firing the laser while adjusting the high voltage discharge.

Once the beam energy was adjusted, the stopper was removed, the lab darkened, and the laser shot made. Plasma formation was determined by recording the laser-target interaction with a polaroid camera. If there was light emitted from the surface, plasma was formed. Type 667 film was used due to its sensitivity to light (3000 ASA). The camera shutter was held open by a remote cable release for approximately one second before and after the shot.

#### 5. Evaluation of Target Surface Damage

Targets were prepared for SEM evaluation as previously described in the section on target preparation. The SEM and electron back scatter detection for topographical analysis, were invaluable in the analysis of surface damage. The optical microscope analysis was not able to provide high enough magnification for analysis of arcing craters (highest available magnification was 600x).

### E. EXPERIMENTAL ERROR

To determine the usefulness of this experiment, an accurate assessment of the experimental error involved is necessary. This requires a thorough understanding of the various sources of error.

The multimode optic that is standard with the Lumonics 822-HP CO<sub>2</sub> laser did not provide a Gaussian distribution of the energy in the beam. It did produce a pulse shape that was constant throughout the experiment (when properly aligned). However, its energy distribution was only approximately uniform and did contain areas of higher energy concentration (hot spots). Due to these non uniformities, the energy distribution was conservatively estimated to induce an error of  $\pm 10\%$ . As discussed earlier in the chapter the uncertainty of the laser energy meter was  $\pm 5\%$ .

Other potential sources of error included the NaCl window calibration, optical device transmittance and reflectance, and the spot size measurement. Each of these sources was conservatively estimated to be  $\pm 2\%$ .



If these uncertainties were all additive the total uncertainty would be  $\pm 23 \%$ . This is an unlikely occurrence and not indicative of the experimental results obtained.

A more accurate analysis of the experimental error is obtained by assuming that each potential source of error is independent of the other sources. Then the method outlined by Holman [Ref. 28] and given by equation 3.2 can be used.

$$U_{\text{tot}} = \{ U_1 + U_2 + U_3 + \dots \} \quad (\text{eqn 3.2})$$

where

$U_{\text{tot}}$  = total expected uncertainty

and  $U_n$  = independent uncertainties.

Substituting into equation 3.2 for the independent uncertainties, an error of  $\pm 11.87 \%$  was obtained.

In view of this analysis, a composite experimental error of  $\pm 12 \%$  was chosen.

## F. EXPERIMENTAL LIMITATIONS

### 1. Beam Nonuniformities

As described in the section on experimental error, the energy distribution of the beam was non-Gaussian. This is a function of the standard multimode optic of the laser. This introduced uncertainty estimated to be  $\pm 10 \%$ . This source of error could be drastically reduced with an unstable resonator to produce a Gaussian beam energy distribution.

### 2. Laser Pulse Duration

Due to considerations concerning damage to the ZnSe beam splitter, a pulse duration of 4.55  $\mu\text{sec}$  was directed to be used throughout the experimentation. This prevented an examination of the laser damage mechanism as a function of pulse duration. The results of the experiment were compared with the results of previous experiments which used a neodymium (1.06  $\mu\text{m}$ ) laser. The pulse duration of this laser was 25 nanoseconds. The fact that the pulse duration was several orders of magnitude shorter than the  $\text{CO}_2$  laser, and that there were two variables involved in this comparison, pulse length and wavelength, made it difficult to make an accurate comparison.

### **3. ZnSe Vacuum Chamber Window**

As discussed previously, the failure of the ZnSe window at much lower power densities and energy fluxes, than the expected damage threshold, caused some delay and much inconvenience. This necessitated obtaining and using NaCl windows for the vacuum chamber.

### **4. Target Orientation**

To prevent the reflection of the laser energy back into the laser output optics, the targets were oriented 3-5 degrees from normal incidence. It should be noted that this differs with the theoretical model. The  $\lambda/4$  relationship for maximum intensity of the E field and plasma production, is still closely approximated by this experimental arrangement. It should also be noted that the  $\lambda/4$  factor was only used as a representative distance to facilitate calculation of the approximate E field magnitude. This experimental limitation was not considered significant.

### **5. Laser Chill Water Unit**

The Flowrite Recirculating Cooling System malfunctioned on 6 occasions. It was out of service for an average of 1-2 days per occurrence. Since the laser could not be operated without the cooling unit, this caused significant delays. It should be noted that the cooling unit was not designed for use with this laser and was probably not designed to handle the high heat loads associated with several hours of operation of a high energy laser system.

### **6. Vacuum Chamber Mechanical Pump Exhaust**

The exhaust of the mechanical pump for the vacuum system did not have a filter on it. This type of system exhausts a small amount of oil when it is in operation. This oil can easily settle on the delicate optics used with the laser, and enhance energy coupling into the surface of the optics. This can cause the optics to fail at much lower energy densities than they were designed to withstand. To prevent this, the enclosure area was thoroughly cleaned and a temporary exhaust line installed to exhaust the oil fumes outside the enclosure.

## IV. EXPERIMENTAL RESULTS

### A. DETERMINATION OF PLASMA ONSET IN VACUUM

A total of twenty-five SS 304 stainless steel targets were irradiated in  $\sim 10^{-6}$  Torr vacuum with a focussed beam  $\text{CO}_2$  pulsed laser. Of these twenty-five targets, eighteen exhibited unipolar arcing. All eighteen of the targets with arcing craters had exhibited plasma formation when the target was irradiated, the seven targets without arcing craters did not exhibit plasma formation. The seven targets that did not display plasma formation, showed no damage to the target surface.

The power density required for plasma onset and arcing was determined to be  $0.41 \pm 12\%$  MW/cm<sup>2</sup>. These results are summarized in Table 6. The error of  $\pm 12\%$  allows for nonuniformities (hot spots) in the beam, and procedural and equipment inaccuracies.

### B. BEAM INACCURACIES

Targets 1 through 10 were unknowingly irradiated using a non-optimal beam shape. This change in the beam shape was due to a change in the temperature in the lab facility (see Chapter III). The beam appeared to be uniform on the laser "show" paper. However, after the power density calculations were made, the results did not agree with the amount of damage on the target surfaces, and there was plasma formation at power densities well below those found for a non-focussed beam [Ref. 14: p. 80]. Examination of these targets with the SEM showed heavy thermal effects and arcing craters typical of much higher power densities.

At this point a more sensitive "show" paper was used, and it became clear that there was a high concentration of the beam energy in a very small portion of the beam. A realignment of the laser optics was performed and the beam returned to its optimal shape. The experimental results for the rest of the targets were in the power density range expected.

The results of the SEM examination of targets 1 through 10 were interesting enough to warrant an approximation of the power densities in the hot spot of the beam, and further examination of the damage done to the surface.

To determine an approximate power density in the hot spot area, the total area that experienced unipolar arcing, on the highest power density target, was determined.

This area was determined to be  $0.1 \text{ cm}^2$ . This area was then subtracted from the total area of the beam giving  $0.899 \text{ cm}^2$ . Then, using the results of the plasma onset experiment, which concluded that if the power density exceeded  $0.41 \text{ MW/cm}^2$  arcing will occur, it was assumed that the  $0.899 \text{ cm}^2$  area had a power density of  $0.41 \text{ MW/cm}^2$ . From this, the ratio of the beam energy in the hot spot was determined, and the per cent of the beam energy in the hot spot calculated. This resulted in an approximation of 62% of the total beam energy being concentrated into the  $0.1 \text{ cm}^2$  area hot spot. Although this sounded very high, it was consistent with the results on targets 1 through 10. In particular, target number 6, which had the lowest beam energy incident on it, and a calculated power density of  $0.236 \text{ MW/cm}^2$ , exhibited thermal effects and cratering more typical of those observed at power densities of  $1.5 \text{ MW/cm}^2$ . This concurred with the approximated value of the power density for the hot spot of  $1.4 \text{ MW/cm}^2$ . The approximated values for the power densities ranged from  $1.4 \text{ MW/cm}^2$  to  $5.9 \text{ MW/cm}^2$  for targets 1 through 10 and the results are listed in Table 6.

## C. TARGET SURFACE DAMAGE

### 1. High Power Densities

The concentration of 62 % of the beam energy in a  $0.1 \text{ cm}^2$  area on targets 1 through 10, had the same effect as using a very tightly focussed beam. The purpose of this experiment was to determine the power density required for plasma onset, so target 1 was irradiated at what was thought to be a power density slightly above the plasma formation threshold (based on the results for an unfocussed beam [Ref. 14: p. 80] ). As explained in the previous section, this resulted in a much higher power density than expected. This caused a much brighter plume of plasma from the target, and subsequently targets 2 through 10 were irradiated with decreasing power densities in an attempt to get below the plasma onset level. Figure 4.1 shows the bright plume of plasma from the target and illustrates the excellent results obtained with the polaroid camera used to determine if plasma was formed. Enough light was emitted from this target's plasma to illuminate the other targets on the wheel with high detail. The screws holding the targets in place are also clearly visible. This picture was taken using 3000 ASA film with an f stop of 11.



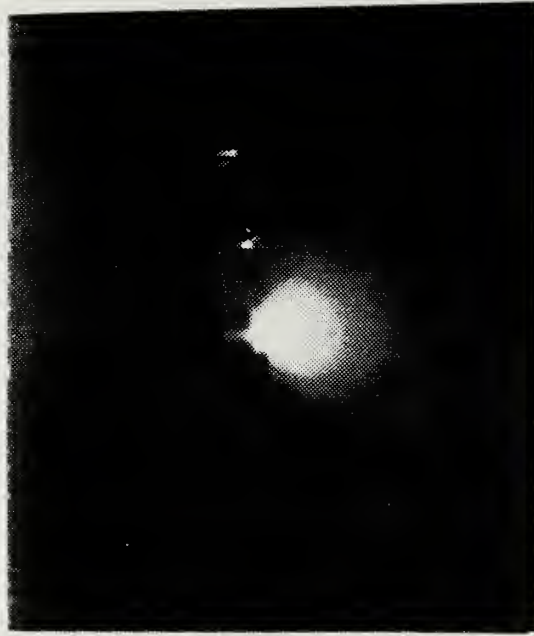


Figure 4.1 Plasma Plume from Laser/Target Surface Interaction  
(High Power Density).

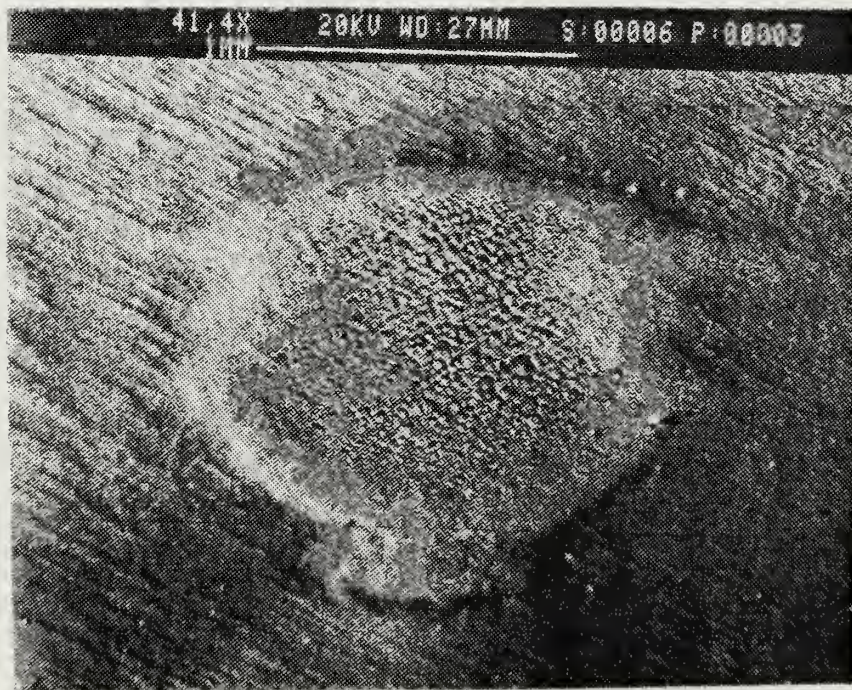


Figure 4.2 Hot Spot Damage at 41.4x Magnification with the SEM.



These high power densities caused surface damage that was visible with the unaided eye. The outline of the area that had unipolar arcing is clearly visible. Figure 4.2 shows the outline of the damaged area under low magnification (41.4x) with the SEM. Even at this low magnification, the arcing craters are distinguishable.

In the center of the hot spot, the craters were very wide, indicative of a long burn duration. There were also heavy thermal effects with the surface showing indications of a change in the grain structure (a phase change) of the stainless steel. The change in the structure of the surface material, indicated that the metal in that area had been heated to a very high temperature and cooled rapidly. This explained the slightly raised appearance of the edges around the heavily damaged areas.

The arcing craters in the center of the hot spots were up to 125  $\mu\text{m}$  across, with cathode spots of up to 14  $\mu\text{m}$ , located in the center of the crater. This indicated that the arcs were well developed and long burning. The longer the arc burned, the more molten surface material was pushed outward to expand the crater rim. Figure 4.3 shows the well developed long burning craters found in the center of the hot spots. The cross-hatched appearance of the surface was caused by the change in the surface grain structure. The craters also appear to run together, this is to be expected with the molten surface material filling in craters as it expands. This overlap of craters is easily seen in Figure 4.4. Because of this it was impossible to get a meaningful crater density count in the hot spots.

Another interesting phenomena was the rapid decrease in crater size and density near the edges of the hot spot as seen in Figure 4.5. This rapid decrease indicated that the arcs near the edge had not burned as long. The lack of a phase change in the surface of the material at the extreme edges of the hot spot substantiated this conclusion. At the edge, the craters were 3-5  $\mu\text{m}$  across, with well formed rims but had no indication of thermal effects.

These results are explained by noting that as the plasma expands outward, it will also cover more of the surface area of the target. As it expands, if the  $T_e$  is high enough at the edges, arcing will occur there. This agrees completely with the Schwirzke model explained in Chapter II.





Figure 4.3 Center of Beam Hot Spot at 326x  
The Large Crater at Upper Right was 125  $\mu\text{m}$  Across  
Cathode Spot was 14  $\mu\text{m}$ .

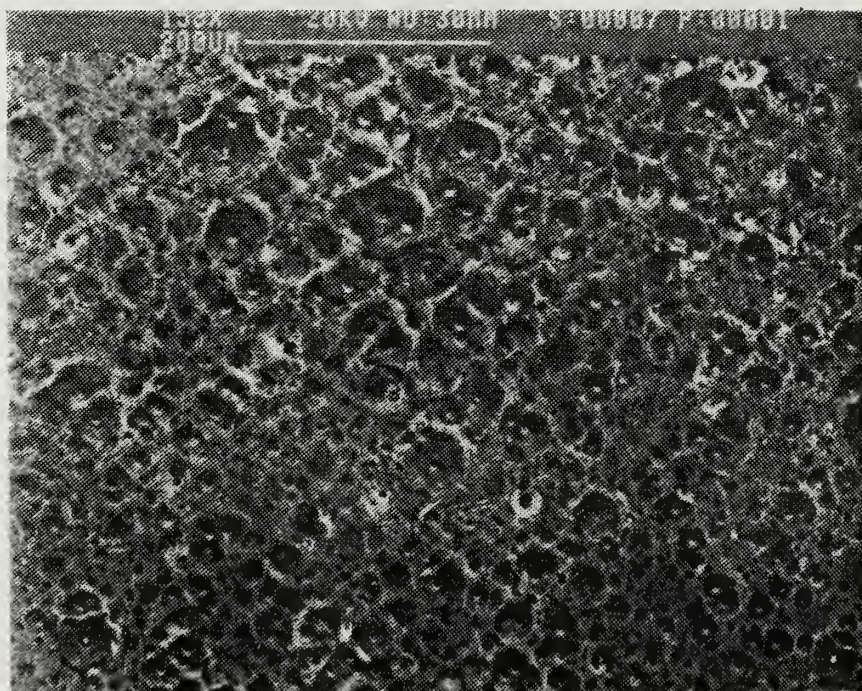


Figure 4.4 Center of Hot Spot, Craters Overlap and Run Together.



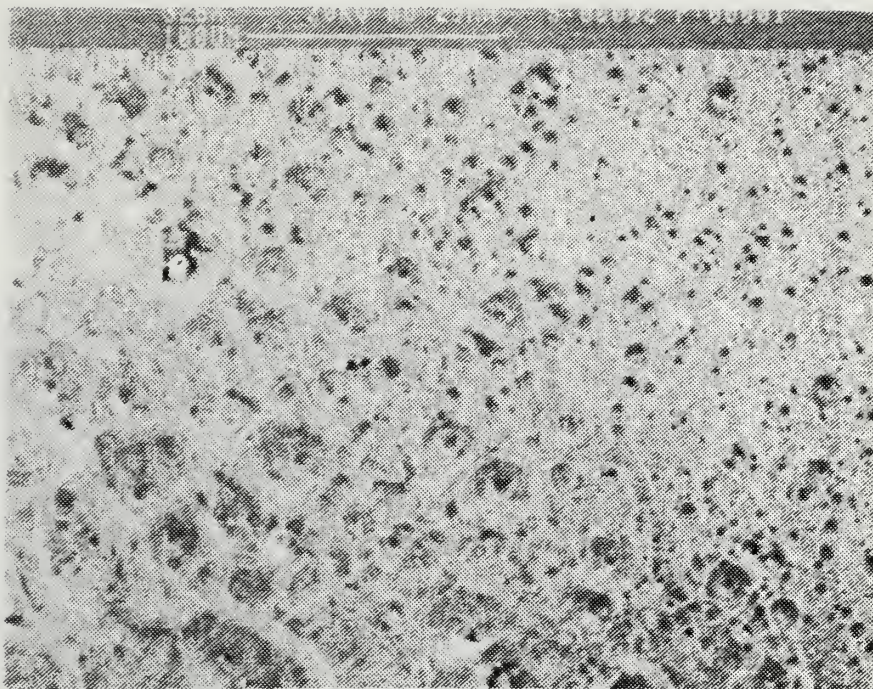


Figure 4.5 Crater Size and Density Near the Edge of the Hot Spot.

## 2. Thermal Effects

Figure 4.6 was representative of the polished targets surface before irradiation using the SEM. Figure 4.7 was representative of the grain structure of the unirradiated target surface, after etching and using an optical microscope. This structure was typical of the Austenite grain structure of the SS 304, one of several phases possible for the composition of SS 304 (18-20 % Cr, 8-10 % Ni, less than 0.8 % C and the rest Fe). The particular phase that the material finally produces depends on the temperature that the mixture was subjected to and the rate at which it was cooled. Austenite, because of its excellent mechanical properties, is the phase of SS 304 that is commercially produced. Figure 4.8 and Figure 4.9 were typical of the thermal effects observed in the high power density areas. After etching it became clear that the surface of the target had changed grain structure, representing a different phase of the SS 304 composition. Figure 4.10 was representative of this phase change. By examining a continuous cooling curve and an equilibrium phase diagram [Ref. 29: p. 11-5], it was possible to determine that the surface in this area had been heated to  $\sim 1450^{\circ}\text{C}$  and cooled in less than 10 seconds. This resulted in a change in the structure of the stainless steel from Austenite to Ferrite and Austenite. The new structure had



less desirable mechanical properties, more brittle, more susceptible to corrosion and stress than the original Austenite grain structure.

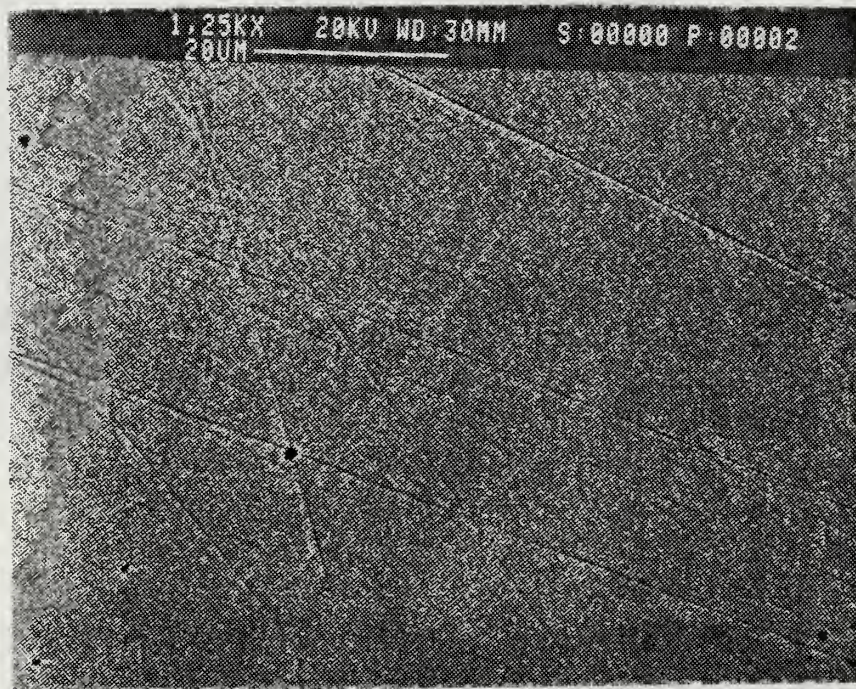


Figure 4.6 Unirradiated Surface  
1250x.

The cross section of the targets revealed that the change in the structure extended to a depth from 8 to 13  $\mu\text{m}$ . The depth depended on the depth of the craters. Craters were from 5-10  $\mu\text{m}$  in depth with the phase change extending  $\sim 3 \mu\text{m}$  below the bottom of the crater.

By etching the surface it was also observed that the unipolar arcing process caused a highly localized deposition of the energy from the plasma. Figure 4.11 was taken at the edge of a hot spot. It was observed that the arcing craters had changed structure but that the surrounding surface had not. This indicated that the energy had been deposited in the crater area, not evenly distributed over the surface of the hot spot.



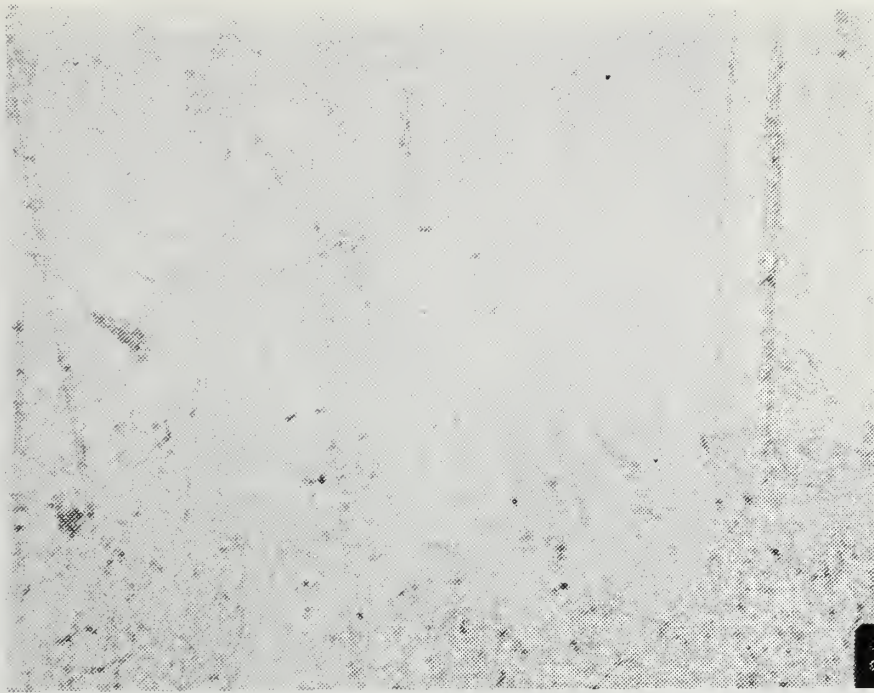


Figure 4.7 Unirradiated Surface After Etching, Optical Microscope  
500x.

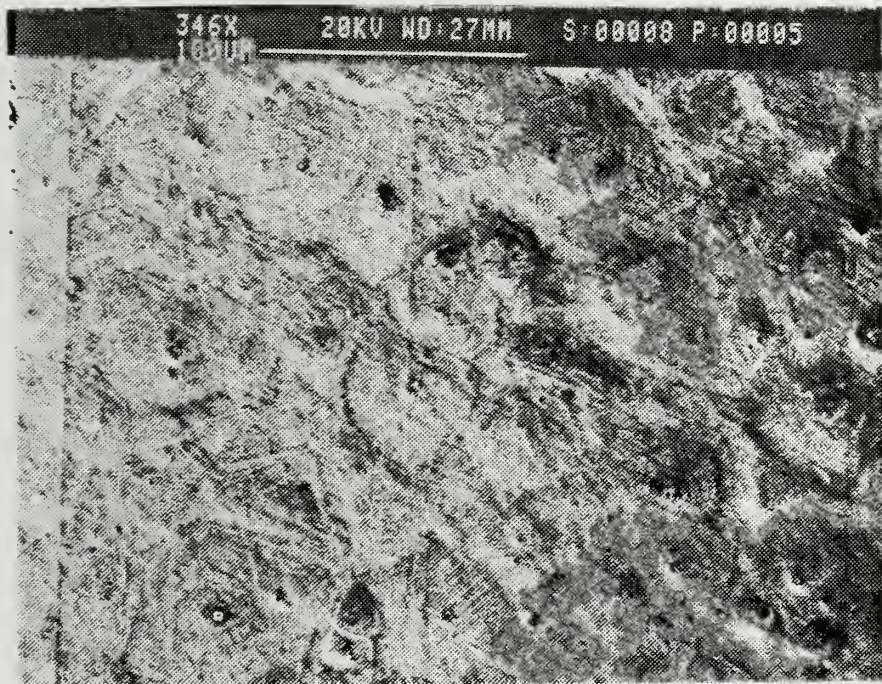


Figure 4.8 Thermal Effects in Beam Hot Spot  
SEM 346.



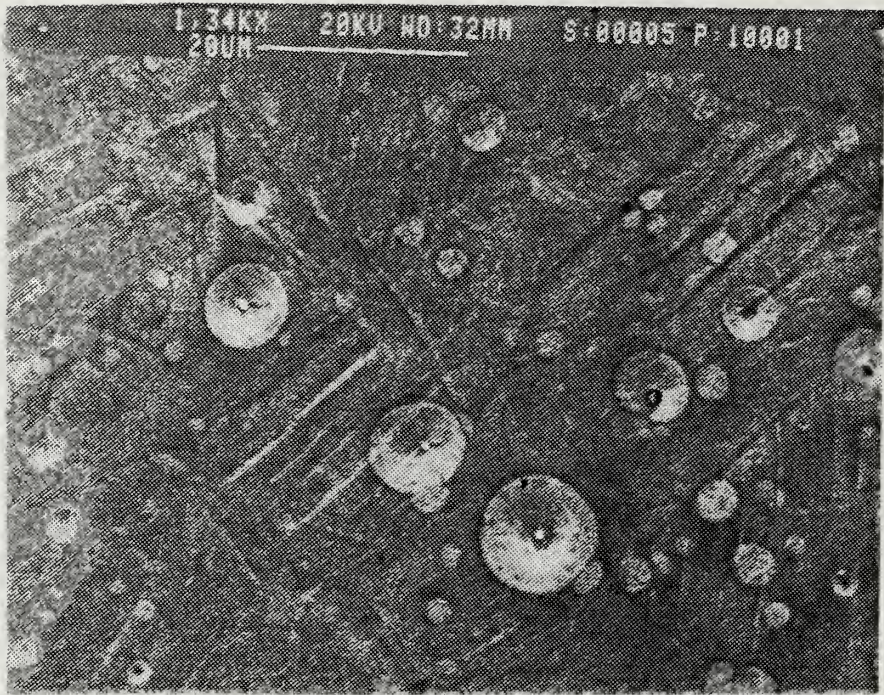


Figure 4.9 Thermal Effects in Beam Hot Spot  
SEM 1340x.

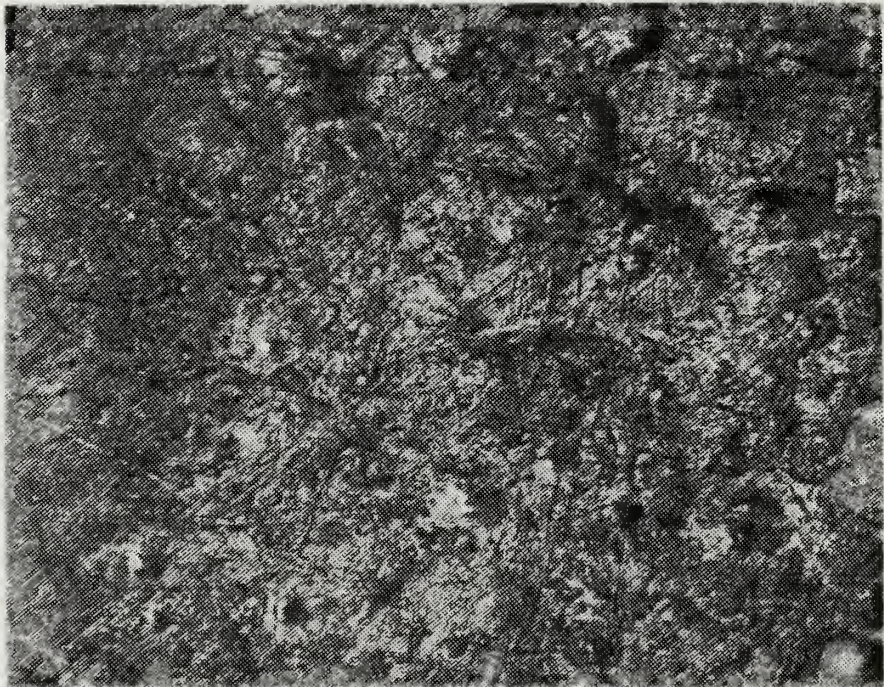


Figure 4.10 Thermal Effects in Beam Hot Spot, After Etching  
Optical Microscope  
500x.



### 3. Low Power Density

After the laser optics were realigned, and starting at the lowest power density calculated ( $0.263 \text{ MW/cm}^2$ ) for the irregular beam, without taking into account the hot spot concentration, targets 11 through 15 were irradiated at increasing power densities. This was done to ensure that the normal focussed beam did not have plasma onset power densities that low. The power was increased until plasma was formed. Targets 11 through 14 had no plasma formation. Target 15, with a power density of  $0.486 \text{ MW/cm}^2$ , indicated plasma formation.

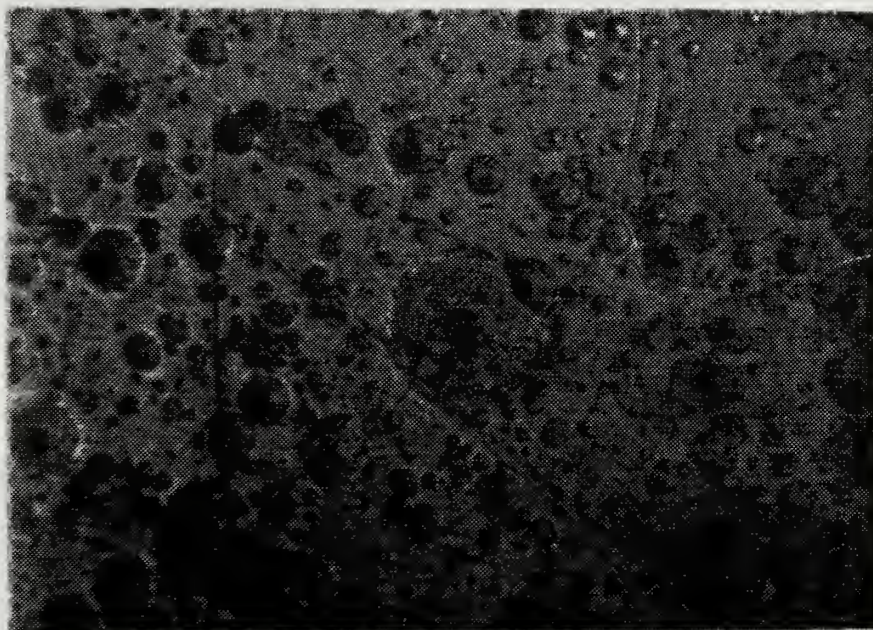


Figure 4.11 Etched Craters at Edge of Hot Spot  
Localized Energy Deposition Caused Local Phase Change  
Optical Microscope 500x.

The size and appearance of arcing craters at low power densities differed significantly from those at high power densities. This difference was attributed to the fact that the arcs did not burn as long. As the power density for arcing onset was approached, thermal effects no longer appeared, and the size of the craters was much smaller.

Figure 4.12 shows a typical arc crater at power density of  $0.559 \text{ MW/cm}^2$ , well above the plasma onset level. Craters range from  $3\text{-}7 \mu\text{m}$  across. The cross-hatched appearance of the surface indicates that thermal effects were present. The crater rim is flat and not raised above the surface, indicating that the surface was molten.



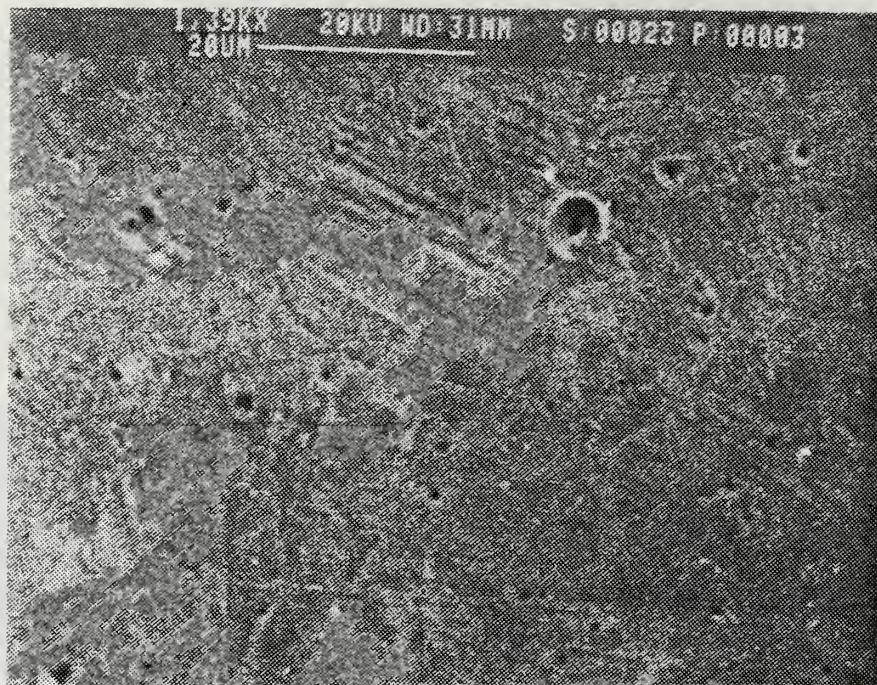


Figure 4.12 Typical Arc Crater at  $0.559 \text{ MW/cm}^2$   
1390x.

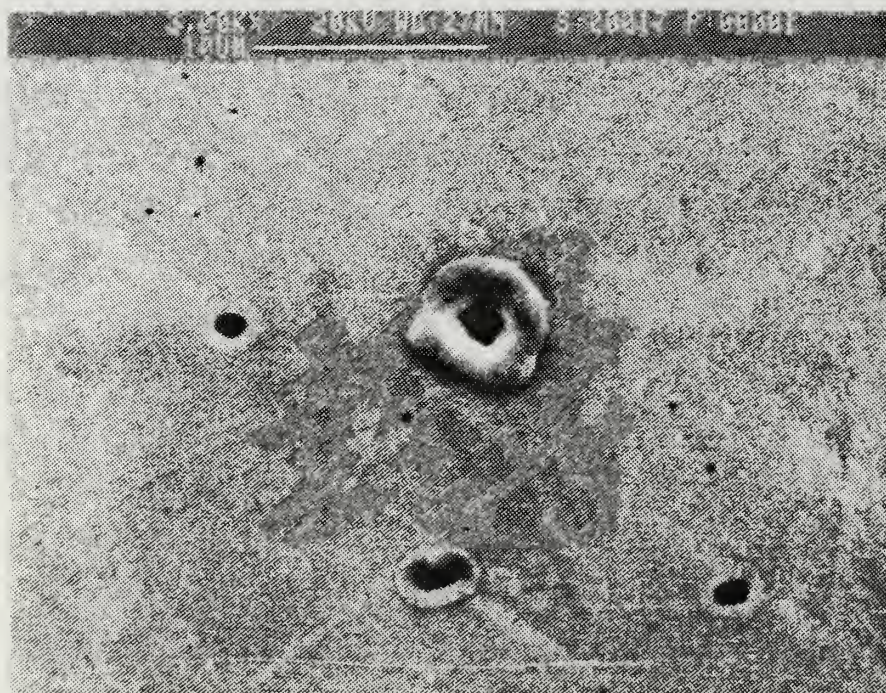


Figure 4.13 Typical Arc Crater at  $0.499 \text{ MW/cm}^2$ , Slightly Above Plasma Onset  
3000x.



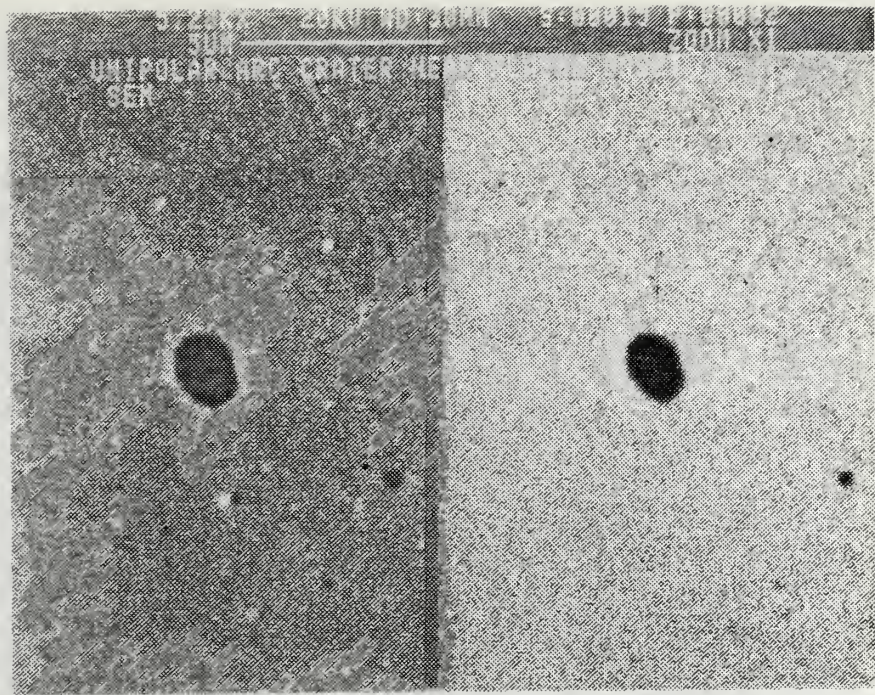


Figure 4.14 Small Arcing Crater Near Plasma Onset  
BSE Conformation on the Right  
5280x.

Figure 4.13 shows a crater at  $0.499 \text{ MW/cm}^2$ , slightly above the plasma onset level. Craters are  $3\text{-}7 \text{ }\mu\text{m}$  across. The crater rim is well formed and raised from the surface indicating that as the molten metal was pushed out of the crater it cooled to form the rim. The surface around the crater did not change phase, indicating that the rest of the surface was not molten.

As the power density was decreased to the plasma onset level, it became increasingly difficult to distinguish small weakly formed craters from small holes left in the surface from carbides, sulfides and manufacturing imperfections. The carbides and sulfides were removed from the surface during the polishing process leaving holes. It was at this point in the experiment that the topographical analyzer feature of the electron Back Scatter Detector (BSE) became invaluable. These small imperfections had the appearance of having rims caused by the charging of the lip of the hole by the electrons. Arcing craters had the same appearance on the SEM, but when the topographical feature of the BSE was used, the false rim disappeared on the holes. Arcing craters had a brighter ring (raised portion) on the BSE confirming the presence of a rim. Figure 4.14 shows a small crater, near plasma onset, on the left and BSE confirmation of its raised rim on the right.



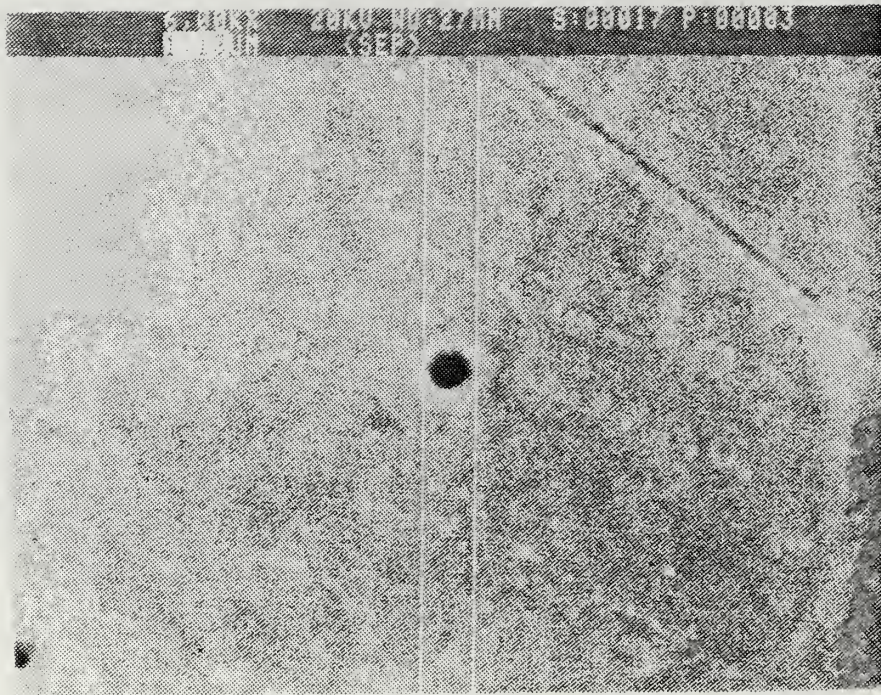


Figure 4.15 Small Weakly Formed Crater  
Near Plasma Formation Power Density  
6000x.

Targets 16 through 20 were irradiated at power densities between  $0.509 \text{ MW/cm}^2$  and  $0.453 \text{ MW/cm}^2$  in an attempt to locate the exact power density for arcing onset. These targets all showed signs of arcing and plasma formation. It should be noted that it was extremely difficult to lower the energy content of the laser pulse with the kV adjustment at these low power levels.

As the power density approached plasma onset, the arcing craters became smaller and sparser. Craters ranged from 1 to  $5 \text{ }\mu\text{m}$  across with weakly formed rims, and cathode spots from 1 to  $3 \text{ }\mu\text{m}$  across. Figure 4.15 shows a  $1.13 \text{ }\mu\text{m}$  diameter crater, with a  $0.9 \text{ }\mu\text{m}$  cathode spot, near the plasma formation power level.

The arc crater in Figure 4.16 had a well formed rim and easily distinguishable cathode spot which was typical of the craters found at power densities just slightly above plasma onset and above.



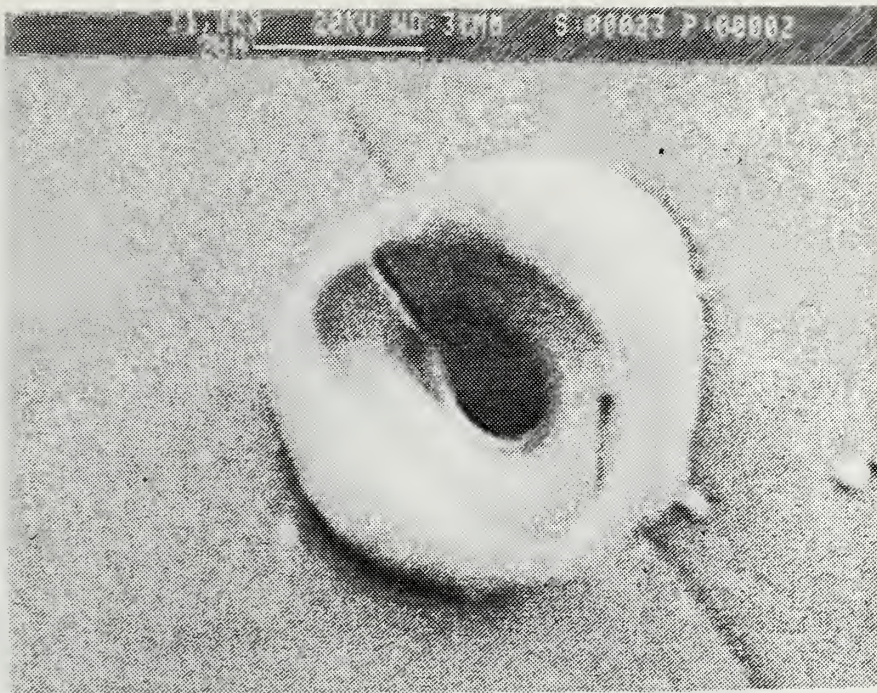


Figure 4.16 Typical Unipolar Arc Crater  
11,100x.

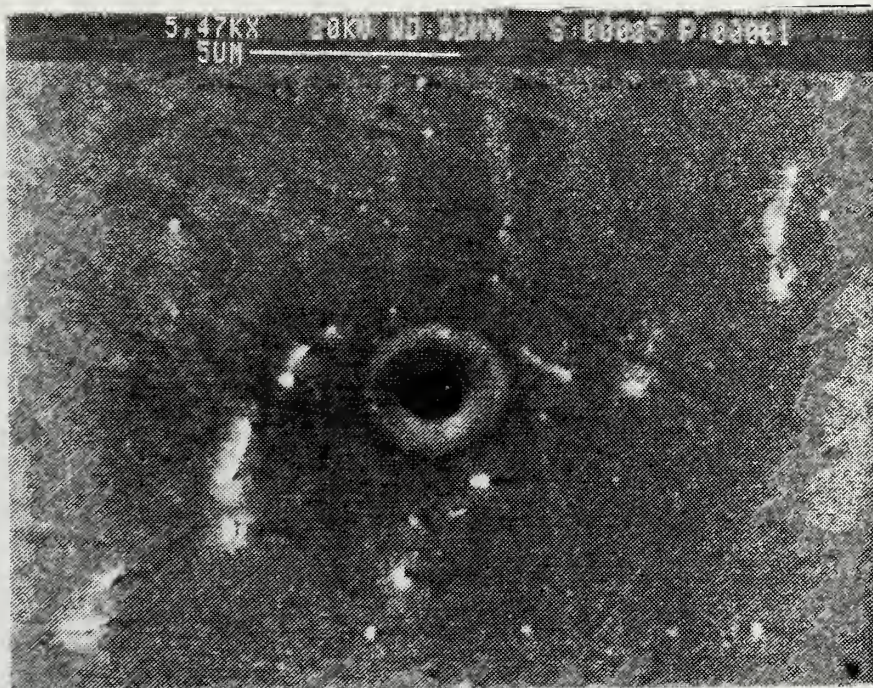


Figure 4.17 Explosively Vaporized Crater at Plasma Onset  
Power Density:  $0.41 \text{ MW/cm}^2$   
5470x.



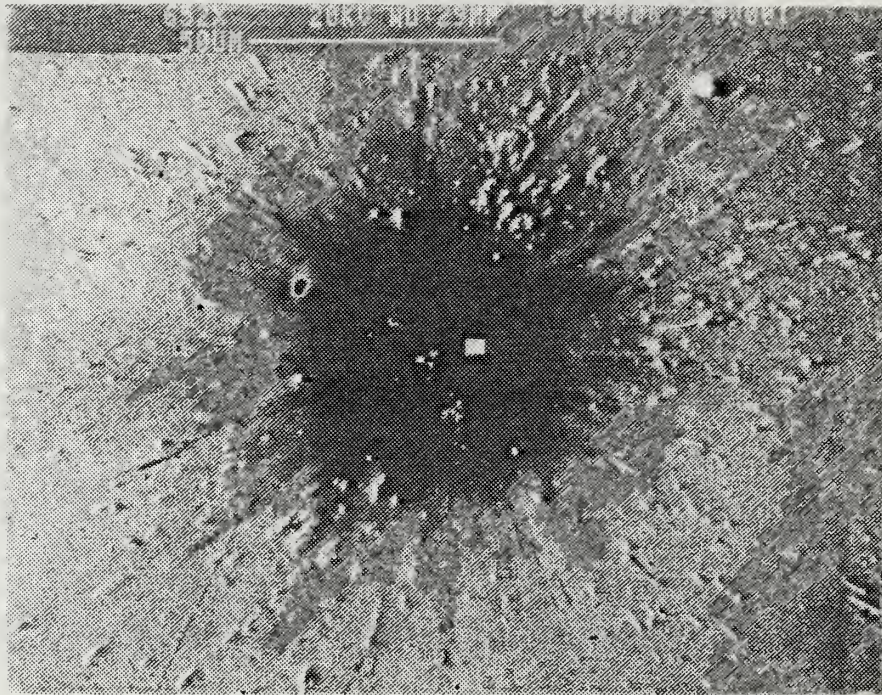


Figure 4.18 Explosive Vaporization of a Surface Imperfection  
652x.

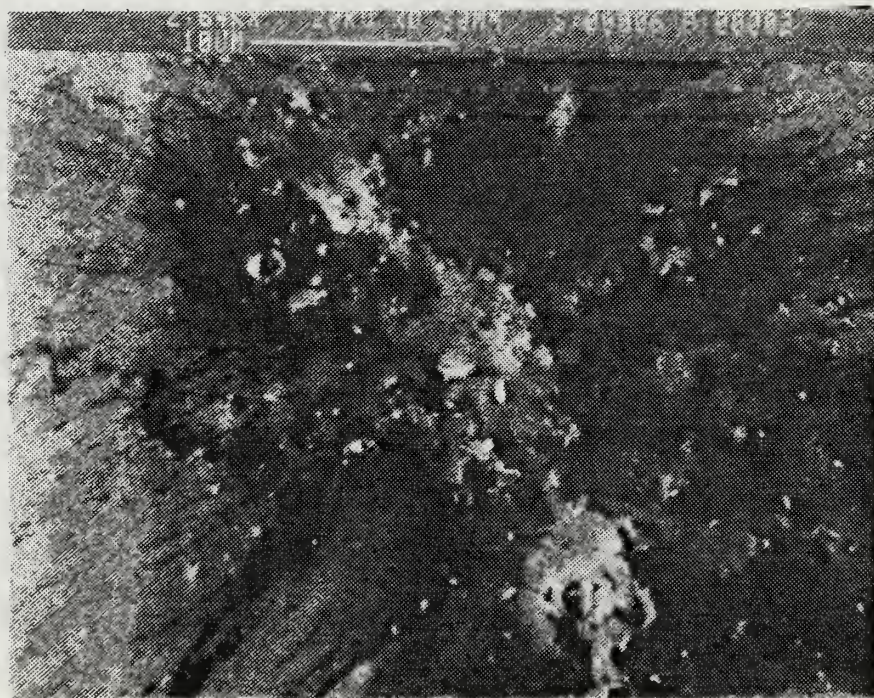


Figure 4.19 Closeup of Vaporized Area  
2,640x.



Targets 22 through 25 were irradiated at power densities around the arcing onset level, to confirm the exact power density of arcing onset. Target 25 was irradiated with a power density of  $0.41 \text{ MW/cm}^2$ . After a painstakingly thorough two hour search of the target surface, fewer than 100 arc craters were found. In conjunction with the results of targets 11 through 25, and the characteristics of the craters that were found, very small craters with weakly formed rims, this power density was determined to be the unipolar arcing onset density. Figure 4.17 shows one of the few craters found on target 25. Note that the rim was barely formed, and the surface near the crater exhibited cooled droplets of metal around it. These droplets indicated that this crater was formed as a result of the explosive vaporization of a whisker, with some of the surface material being ejected from the crater and cooling on the surrounding surface. The fact that these droplets (which had become whiskers themselves) did not in turn vaporize, indicates that the power density was just barely sufficient to bring on arcing before the laser pulse ceased.

Explosive vaporization of a whisker was more dramatically illustrated by Figure 4.18 and Figure 4.19. These pictures were taken on target number 6 at the edge of the hot spot. A relatively large quantity of surface material was vaporized in an explosive manner, sending droplets of surface material in all directions. Figure 4.19 shows a close up of the area where the vaporization occurred. Several clearly visible unipolar arc craters were noted in this area. It is not obvious if this area was a droplet of molten material ejected from the center of the hot spot, or a whisker that vaporized explosively, and the droplets ejected from it continued the process causing more explosive vaporization. The darkened area was caused by surface charging effects.

#### **D. ZINC SELENIDE WINDOW**

As mentioned in Chapter III, the ZnSe window purchased for use with the vacuum chamber was damaged at well below its expected damage threshold. According to Ready [Ref. 18: p. 153] experimentation with ZnSe confirmed its ability to withstand laser pulse energy levels in the  $27\text{-}41 \text{ joules/cm}^2$  range for a 600 nanosecond pulsed  $\text{CO}_2$  laser. Window damage due to thermal runaway occurred during testing at an energy density of approximately  $5 \text{ joules/cm}^2$ , well below the expected damage threshold. Subsequent examination of the damage showed unipolar arc craters in the damaged area. The ZnSe window was coated with an anti-reflective coating to prevent radiation reflecting back into sensitive optics. For proprietary

reasons the manufacturer of the window would not divulge the exact nature of the anti-reflective coating, but did indicate that it should have withstood the energy to which it was subjected. Figure 4.20 is a photograph of the damaged area on the window taken through an optical microscope. Unipolar arc craters are clearly visible at this level of magnification (500x) which indicated that the craters were quite wide. Close examination of the edges of the damaged surface indicated that the anti-reflective coating had broken down, apparently before the ZnSe substrate had been damaged. Once the coating had broken down, it became a contamination on the surface of the ZnSe substrate. This enhanced the energy coupling into the ZnSe which resulted in breakdown well below the predicted damage threshold. It was impossible to determine if the anti-reflective coating broke down due to an imperfection in the coating or more likely, if there was some contamination of the surface (finger-print oils, dirt, etc.). The NaCl windows that were used to replace the ZnSe window, performed well with power densities as high  $7 \text{ joules/cm}^2$  and could probably have withstood energy levels to  $45 \text{ joules/cm}^2$  [Ref. 18: p. 153].

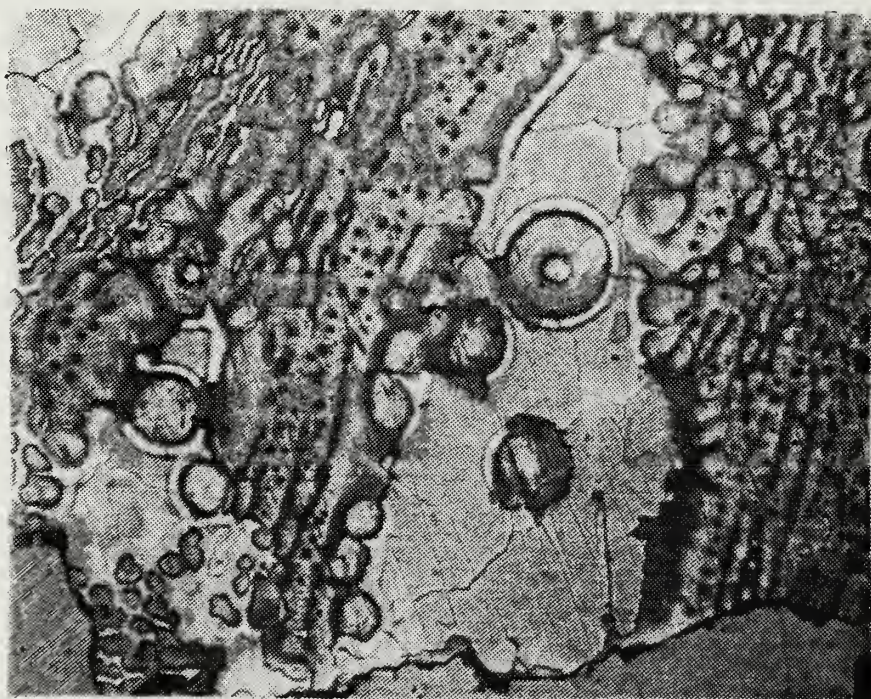


Figure 4.20 ZnSe Window with Unipolar Arc Damage  
500x.



## E. DISCUSSION OF RESULTS

### 1. Introduction

To add completeness and continuity to this study, a comprehensive evaluation of the experimental results presented in this chapter and a qualitative comparison of these results with the results of previous studies was undertaken.

### 2. Qualitative Comparison of Previous Results

Beelby and Ulrich [Ref. 10] conducted a similar experiment in 1981. Before comparing these results with this experiment, it was necessary to review the differences in the experiments. Beelby and Ulrich used a Q switched Korad 1500 neodymium glass laser with a wavelength of 1.06  $\mu\text{m}$ , and a pulse length of 20 nanoseconds. Both experiments were similar in that they irradiated SS 304 targets in a  $10^{-6}$  Torr vacuum with a focused beam. This experiment used a Lumonics CO<sub>2</sub> TEA high energy pulsed laser with a wavelength of 10.6 microns and a pulse length of 4.55  $\mu\text{sec}$ . It was significant that the wavelength of the CO<sub>2</sub> laser was 10 times the wavelength of the neodymium laser, and that the pulse duration of the CO<sub>2</sub> laser was over 200 times that of the neodymium laser.

Beelby and Ulrich examined 10 SS 304 targets over a relatively wide range of power densities (5.4 MW/cm<sup>2</sup> to 64.4 MW/cm<sup>2</sup>). Only 2 of their targets were dedicated to determining the plasma onset power density. As reported at the beginning of this chapter, 25 targets were irradiated over a narrow range of power densities, specifically trying to find the plasma formation threshold.

Beelby and Ulrich estimated that the plasma formation power density for SS 304 in a vacuum was 5.4 MW/cm<sup>2</sup>. This indicated that this was an order of magnitude approximation because of a variety of experimental limitations. The plasma formation threshold for SS 304 reported herein was 0.41 MW/cm<sup>2</sup>  $\pm$  12 %. The difference in the plasma formation power densities was attributed to the difference in wavelength and particularly to the difference in pulse duration, with a resultant difference in laser/surface energy coupling.

Although the reported power densities for plasma formation differed by an order of magnitude, there were some striking similarities in the results. Experimental results in both studies proved conclusively that unipolar arcing constituted the dominant laser damage mechanism at power densities near plasma formation threshold. They also proved that there was no surface damage without plasma formation and that plasma formation was necessary for the initiation of unipolar arcing. Additionally the



size of the unipolar arc craters at plasma onset for both studies was 1-2  $\mu\text{m}$  in diameter with distinct, symmetric rims.

### **3. Comparison of Focused and Unfocused Beam Experimental Results**

The results of a concurrent study using an unfocused beam, done by Olson [Ref. 1] concluded that the power density for plasma formation in a  $10^{-6}$  Torr vacuum was  $0.43 \text{ MW/cm}^2 \pm 12 \%$ . Olson's study used a  $2 \text{ cm}^2$  spot size. This threshold for plasma formation was consistent with the experimental results reported herein.

## V. CONCLUSIONS AND RECOMMENDATIONS

The primary purpose of this study was to determine the power density required for plasma production for SS 304 stainless steel and to investigate the laser damage mechanism. This was accomplished by the detailed examination of the plasma-surface effects on the target surfaces. The targets were irradiated with a CO<sub>2</sub> pulsed laser with a focused beam of approximately 1 cm<sup>2</sup> in a 10<sup>-6</sup> Torr vacuum.

The secondary purpose of this study was to prove the usefulness of the CO<sub>2</sub> laser facility as a student research tool. This was accomplished and the recommended operating procedures and safety requirements were documented in Appendix A. Several necessary test were accomplished to get the laser facility into operation. The results of the laser pulse energy content vs. high voltage setting was documented in graphical form in Appendix A as Figure A1. The results of the laser pulse to pulse energy repeatability study are documented in Appendix B in tabular form.

### A. QUALITATIVE COMPARISON OF EXPERIMENTAL RESULTS WITH THE THEORETICAL MODEL

The theory presented in Chapter II identified evaporation and ion-sputtering as possible sources of laser damage. Although ion-sputtering and evaporation contribute to the plasma formation process, they are not the dominant damage mechanisms. Unipolar arcing was the primary damage mechanism observed in this study. It did not occur without plasma formation and was present whenever there was a plasma formed. The thermal effects noted at power densities above the plasma onset level, were a consequence of the thermal heating of the surface from the unipolar arcing process. These results were completely consistent with the Sequential Unipolar Arcing Model presented in Chapter II.

### B. PLASMA FORMATION POWER DENSITY THRESHOLD

The power density required for plasma formation was determined to be 0.41 MW/cm<sup>2</sup> ± 12 %. To refine the Sequential Unipolar Arc Model into a quantitative model requires further research to determine the plasma density, the T<sub>e</sub> and the V<sub>f</sub> at arcing onset. This would need to be done for several materials with lasers of various wavelengths to ensure completeness of the model. At this stage in its development, the model presents an accurate view of the unipolar arcing process and the sequence of events leading to unipolar arcing.

## C. RECOMMENDATIONS

### 1. Facility Improvements

The nonuniformity of the energy distribution in the laser beam introduced the largest degree of experimental uncertainty. This could be virtually eliminated by the purchase and installation of an unstable resonator for the front end optics of the laser. This would not impact future studies at high power densities as much as it would studies requiring precise power density levels.

The high humidity, dust, and temperature variation in the lab facility will eventually lead to a shorter lifespan for the laser. They will also affect the results of some types of experimentation. For these reasons it is recommended that an attempt be made to build a clean room environment in the lab facility. It would be prohibitively expensive to turn the lab facility into a complete clean room, but a few relatively inexpensive modifications would help enormously. The completion of the air conditioner installation, installation of some sort of disposable filter over the building heat outlets in the room, placing weather stripping around the door, and putting a filter on the mechanical pump for the vacuum chamber would significantly improve the lab environment.

The procurement of a beam splitter less susceptible to damage and that would allow more energy to be transmitted (1-5 %) would improve the performance range of the power meter and allow more versatility in experimentation. The procurement of a short focal length parabolic mirror ( $\sim 15$  cm) would allow focussing of the beam in the vacuum chamber, allowing for higher power density studies in the chamber.

### 2. Possible Future Research

As with many research experiments, this study answered one question and raised several others. Areas of interest that were raised include investigation of the following:

- Plasma density at unipolar arcing onset.
- The magnitude of  $V_f$  and  $V_c$  at arcing onset.
- The effect of varying pulse duration on the power density for plasma onset.
- The effect of multiple pulses and changing the time between pulses, on the damage mechanism and amount of damage done to the surface of the target.
- The effect of having a weakly ionized plasma and a potential between the plasma and the target (as in spacecraft and satellite charging) on the power density required for unipolar arcing onset.

It is strongly recommended that the study of the unipolar arcing process be continued.

## APPENDIX A

### LUMONICS TE-822 HP CO<sub>2</sub> LASER OPERATING PROCEDURE

Although the CO<sub>2</sub> high energy pulsed laser is an excellent research instrument for the study of plasma surface interactions, it must be operated in strict accordance with applicable safety precautions and operating procedures in order to continually ensure the safety of operators and the protection of equipment.

Prior to operating the laser system, an individual must complete a retina scan eye examination to comply with OSHA requirements. Prospective operators must become thoroughly familiar with all procedural and safety aspects of the laser system and receive a systems operation orientation from the Physics Department Plasma Lab Technician and demonstrate the ability to safely operate the system prior to being designated in writing as a laser facility supervisor. It should be noted that at least two individuals, one of whom is a qualified laser facility supervisor, must be present in the plasma laboratory at all times when the laser system is in operation.

Complete awareness of the potential hazards associated with the laser system operation is a necessary prerequisite for prospective laser facility supervisors. One of these hazards arises because the 10.6 micron wavelength of CO<sub>2</sub> is outside of the visible spectrum, and therefore, inadvertent exposure of the eyes and other body parts to the high energy laser beam is a definite possibility if necessary precautions are not routinely enforced. These precautions include the wearing of protective safety glasses by all personnel present in the plasma laboratory during laser system operation and the verification that all openings to the plexiglass experiment area enclosure are shut before firing the laser. The high voltage, resident in the power supplies inside the laser cabinet, presents a potential electrical hazard if safety precautions are not properly heeded. All operators must ensure that the laser cabinet covers are securely in place prior to operating the laser and that any trouble shooting of the electrical system is accomplished only by a qualified technician who completely understands high voltage power supplies and the hazards associated with capacitor discharge. Since the energy content of the laser beam can be quite large, the possibility of a laser induced fire can not be overlooked. This is particularly important when making spot size recordings on paper because the incidence of a series of rapid pulses on the paper will likely ignite it. Therefore, when measuring spot sizes, use single shots spaced at prudent intervals to avoid fires.



The laser is equipped with a variety of system interlocks designed to prevent the operation of the system under conditions which would ultimately lead to personal injury or cause equipment damage. UNDER NO CIRCUMSTANCES will these interlocks be overridden or modified in any manner without the prior notification and consent of the Plasma Lab Technician and the written approval of the appropriate department chairmen with cognizance over the laser facility. These electrical interlocks, which are contained in the laser pulse initiation circuit, include:

- C. Laser Enclosure Cover Interlocks (2) - ensure that electrical shock from the high voltage power supplies and interior electrical components is avoided during laser operation.
- C. Laser Output Port Protective Cover Removed - ensures that the laser is not inadvertently pulsed with the output port protective cover in place causing reflection back into the internal optics and a high probability of damage.
- C. Cooling Water Flow - ensures that proper cooling water flow and pressure are maintained in the laser system so that the temperature sensitive high voltage power supplies do not overheat and fail on thermal overload. Thermal interlocks associated with the high voltage power supplies are designed to trip on temperatures in excess of 125° F.
- C. Laser Power Key - ensures that power is not available to the laser system until consciously applied by the operator.
- C. Gas ON/OFF Switch - ensures that high voltage is not applied to the firing circuit unless gas flow has been properly established in the laser.
- C. Plasma Laboratory Door - ensures that the laser system firing circuit will be temporarily disabled if the laboratory door is opened during laser system operation. The door audible alarm alerts operators of this problem.

Thus, although it can be seen that the interlock system does afford considerable safety, electrical interlocks can never replace the requirement for an alert and conscientious operator. It is with this in mind that the following operational procedure is provided. The basis for the procedural sequence is contained within the Lumonics TE-822 HP Instruction Manual [Ref. &Olson24].

Laser System Start-Up is accomplished by following these sequential procedural steps:

1. Initiate cooling water flow and set the thermostat on the chill water unit to 15 °C.



2. Activate the Laboratory Door Interlock by placing the toggle switch on the control box to the left of the door to the ON position.
3. Set the MODE SELECT switch to SINGLE and the MULTIPLIER setting to X10.

### NOTE

The MULTIPLIER control setting has three positions which are X.1, X1, and X10. These settings are used in conjunction with the INTERNAL RATE potentiometer and apply their stated multiplication factors to establish a desired pulse repetition frequency. In the X1 and X10 positions the capacitors in the laser firing circuit are continuously charged, and the front panel voltmeter continuously registers the high voltage power supply voltage level. In SINGLE shot mode, repetitive pulsing is not possible but the X10 MULTIPLIER setting is used so that the high voltage power supply voltage can be monitored continuously during the conduct of the laser start up procedure.

4. Open the Helium, Carbon Dioxide and Nitrogen cylinder valves and adjust each pressure regulator to 10 psig.
5. Turn the LASER POWER KEY to ON and note that the GAS OFF indicator is GREEN, the INTERLOCKS OPEN indicator is WHITE and the WARM UP INCOMPLETE indicator is YELLOW.
6. Slowly open the HEAD EXHAUST VALVE by placing the valve operator, which is located in the lower right hand corner of the front control panel, in the vertical position.

### CAUTION

Failure to open the HEAD EXHAUST VALVE will cause the Head to quickly become overpressurized. It is equipped with a NON-RESETTABLE 5 psig pressure relief valve. Opening of this relief valve will place the laser system out of commission until a replacement valve is installed.

7. Depress the GAS ON pushbutton and observe that the RED GAS ON indicator is lit while the GREEN GAS OFF indicator is extinguished.

8. After gas flow is initiated, reverify that the three gas bottle regulators are set at 10 psig. Adjust the settings as necessary.

### CAUTION

Consult the Laser Instruction Manual and ensure that only gases of the specified purity characteristics are utilized in the laser system.

9. Adjust the 6 Brooks flowmeters (three on the front control panel and three on the rear panel) to the desired flowrates recommended in the Laser Instruction Manual. Standard long pulse gas settings which are recommended for high voltage power supply settings up to 33 kV and pulse repetition frequencies  $\leq 10$  Hz are 8 SCFH for  $N_2$  and  $CO_2$  and 6 SCFH for He.
10. The INTERLOCKS OPEN indicator should be lit as the warm up proceeds.
11. Allow the gas purge to continue for a minimum of 15 MINUTES if the laser has been shut down for a lengthy period. During periods of frequent operation, a 5 MINUTE purge is adequate to flush the system and is strongly recommended in the interest of conserving gases.
12. Open the air cylinder and set the pressure regulator in the 16-24 psig range and establish a flowrate of 4 SCFH by adjusting the 6 flowmeters on the rear panel.
13. After the WARM UP INCOMPLETE indicator is extinguished (approximately one minute after the application of AC power) and the gas purge has been completed, the INTERLOCKS OPEN indicator will remain lit until the protective cover on the laser output port is removed at which time the INTERLOCKS OPEN indicator will be extinguished.
14. Set the HV CONTROL knob fully counterclockwise to its MINIMUM setting and depress the RED HIGH VOLTAGE ON pushbutton.
15. Turn The HV CONTROL knob clockwise until the voltmeter indicates 26 kV.

### CAUTION

Before commencing to pulse the laser VERIFY that the plexiglass experiment area enclosure is completely closed, that a laser beam absorbing stopper is positioned in the beam path at least one meter away from the output port and that all personnel in the plasma laboratory are wearing protective safety glasses. NEVER allow the high voltage to exceed 40 kV because this will inevitably result in the premature failure of the High Voltage Power Supplies.

16. The laser should now fire each time the SINGLE fire pushbutton is depressed.
17. In the event the laser DOES NOT FIRE, adjust the spark gap air pressure down in small increments until the laser pulses consistently.
18. Turn off the high voltage by depressing the HIGH VOLTAGE OFF pushbutton.
19. Position the MULTIPLIER switch to X.1, the INTERNAL RATE to 5 Hz and the MODE SELECT switch to MULTIPLIER.
20. Depress the HIGH VOLTAGE ON pushbutton and observe the laser pulsing at 0.5 Hz.

The laser is now fully prepared to support experimentation, but before doing so it is recommended that recording paper be used to determine the laser burn pattern. Comparison of this burn pattern with the nominal 30 mm by 33 mm pattern will provide a good indication that the laser is properly aligned and operating satisfactorily.

When the laser system has been secured for a relatively short period of several hours and the gas mix has been preserved in the head, the 15 minute gas purge is not required and a modified START-UP procedure may be employed which consists of the following sequential steps:

1. Turn on AC power.
2. Initiate and verify correct cooling water temperature and flowrate.
3. Open the HEAD EXHAUST VALVE and initiate and adjust gas pressures and flowrates.
4. After completion of warm-up and satisfying conditions to close all interlocks, initiate high voltage. When the GREEN HIGH VOLTAGE OFF indicator lights up, the laser is prepared to operate.

5. Subsequent to the completion of the laser system start up requirements and verification that ALL safety precautions have been met, the laser system may be safely operated.

The graphical depiction of laser pulse energy in joules versus laser high voltage power supply voltage level, contained in Figure A.1, was provided to assist future laser operators in the selection of appropriate experimental parameters. The long pulse gas mixture settings, previously described in this thesis, were used to establish the initial conditions upon which Figure A.1 data was based.



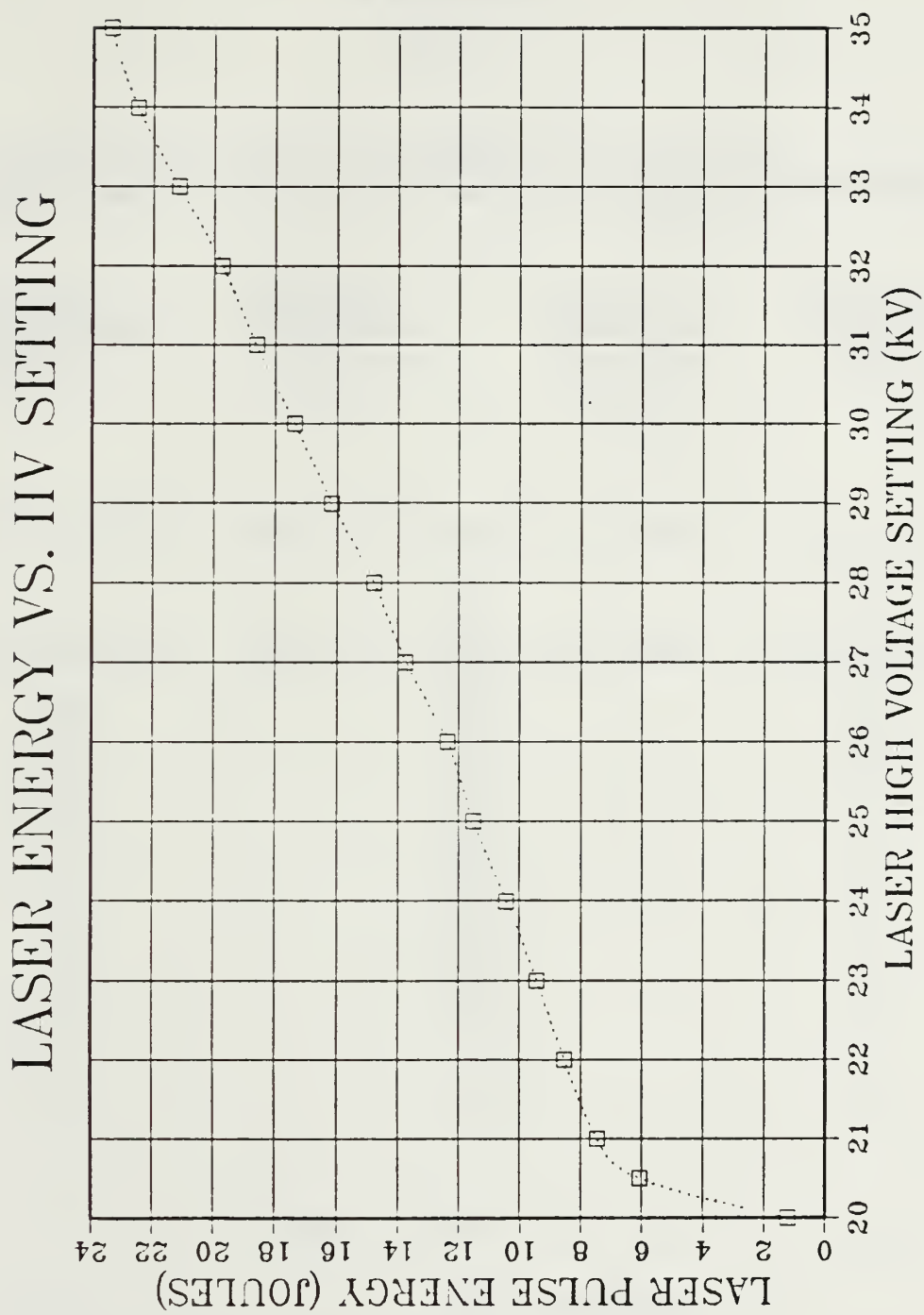


Figure A.1 Laser Pulse Energy Content Versus Laser Power Supply High Voltage Level.

## APPENDIX B

### TABLES

TABLE 1  
LASER PULSE ENERGY REPEATABILITY (27 KV/7100 ENERGY METER)

<i>AIR GAP</i> (psi/SCFH)	<i>NITROGEN</i> (psi/SCFH)	<i>HELIUM</i> (psi/SCFH)	<i>CARBON DIOXIDE</i> (psi/SCFH)
18/6	10/8	10/4	10/8

<i>Laser Shot Number</i>	<i>Energy Meter Reading ( <math>\times 10^{-2}</math> Joules)</i>	<i>Pulse Energy (Joules)</i>
1	1.604	12.34
2	1.621	12.47
3	1.644	12.65
4	1.637	12.59
5	1.648	12.68
6	1.593	12.25
7	1.660	12.77
8	1.597	12.28
9	1.633	12.79
10	1.663	12.79

MEAN = 1.630 12.54

STANDARD DEVIATION = 0.024 0.186

TABLE 2  
LASER PULSE ENERGY REPEATABILITY (27 KV/3232 ENERGY METER)

<i>AIR GAP</i> (psi/SCFH)	<i>NITROGEN</i> (psi/SCFH)	<i>HELIUM</i> (psi/SCFH)	<i>CARBON DIOXIDE</i> (psi/SCFH)
18/6	10/8	10/4	10/8

<i>Laser Shot Number</i>	<i>Energy Meter Reading ( <math>\times 10^{-2}</math> Joules)</i>	<i>Pulse Energy (Joules)</i>
1	1.64	12.62
2	1.60	12.31
3	1.65	12.69
4	1.67	12.85
5	1.68	12.92
6	1.71	13.15
7	1.60	12.31
8	1.66	12.77
9	1.67	12.85
10	1.65	12.69
MEAN = 1.653		12.72
STANDARD DEVIATION = 0.032		0.247



TABLE 3  
LASER PULSE ENERGY REPEATABILITY (28 KV/7100 ENERGY METER)

<i>AIR GAP</i> (psi/SCFH)	<i>NITROGEN</i> (psi/SCFH)	<i>HELIUM</i> (psi/SCFH)	<i>CARBON DIOXIDE</i> (psi/SCFH)
18/6	10/8	10/4	10/8

<i>Laser Shot Number</i>	<i>Energy Meter Reading ( <math>\times 10^{-2}</math> Joules)</i>	<i>Pulse Energy (Joules)</i>
1	1.732	13.32
2	1.807	13.90
3	1.741	13.39
4	1.727	13.28
5	1.734	13.34
6	1.759	13.53
7	1.729	13.30
8	1.754	13.49
9	1.771	13.62
10	1.800	13.85
MEAN = 1.755		13.50
STANDARD DEVIATION = 0.028		0.214

TABLE 4  
LASER PULSE ENERGY REPEATABILITY (28 KV/7100 ENERGY METER)

<i>AIR GAP</i> (psi/SCFH)	<i>NITROGEN</i> (psi/SCFH)	<i>HELIUM</i> (psi/SCFH)	<i>CARBON DIOXIDE</i> (psi/SCFH)
18/4	10/8	10/6	10/8

<i>Laser Shot Number</i>	<i>Energy Meter Reading ( <math>\times 10^{-2}</math> Joules)</i>	<i>Pulse Energy (Joules)</i>
1	1.735	13.35
2	1.796	13.82
3	1.722	13.25
4	1.755	13.50
5	1.757	13.52
6	1.781	13.70
7	1.742	13.40
8	1.759	13.53
9	1.783	13.72
10	1.730	13.31
MEAN = 1.756		13.51
STANDARD DEVIATION = 0.023		0.179

TABLE 5  
LASER PULSE ENERGY REPEATABILITY (33 KV/7100 ENERGY METER)

<i>AIR GAP</i> (psi/SCFH)	<i>NITROGEN</i> (psi/SCFH)	<i>HELIUM</i> (psi/SCFH)	<i>CARBON DIOXIDE</i> (psi/SCFH)
18/4	10/8	10/6	10/8

<i>Laser Shot Number</i>	<i>Energy Meter Reading ( <math>\times 10^{-2}</math> Joules)</i>	<i>Pulse Energy (Joules)</i>
1	2.501	19.24
2	2.574	19.80
3	2.537	19.52
4	2.497	19.21
5	2.566	19.74
MEAN = 2.535		19.50
STANDARD DEVIATION = 0.032		0.245



TABLE 6  
ONSET OF PLASMA FORMATION DATA FOR SS304 TARGETS IRRADIATED  
IN A VACUUM

<i>Target No.</i>	<i>P<sub>d</sub>(MW/cm<sup>2</sup>)</i>	<i>Plasma</i>	<i>Arcing Damage</i>	<i>Thermal Effects</i>
1	5.9*	YES	YES	YES
2	5.2*	YES	YES	YES
3	4.7*	YES	YES	YES
4	4.2*	YES	YES	YES
5	2.6*	YES	YES	YES
6	1.4*	YES	YES	YES
7	2.6*	YES	YES	YES
8	3.0*	YES	YES	YES
9	2.4*	YES	YES	YES
10	2.1*	YES	YES	YES
11	0.115	NO	NO	NO
12	0.224	NO	NO	NO
13	0.260	NO	NO	NO
14	0.358	NO	NO	NO
15	0.486	VERY DIM	YES	NO
16	0.509	DIM	YES	NO
17	0.499	DIM	YES	NO
18	0.469	VERY DIM	YES	NO
19	0.453	VERY DIM	YES	NO
20	0.491	DIM	YES	NO
21	2.741	YES	YES	YES
22	0.266	NO	NO	NO
23	0.559	YES	YES	YES
24	0.317	NO	NO	NO
25	0.409	VERY DIM	YES	NO

\* Indicates that the power density was approximated (see Chapter IV, Beam Inaccuracies).

## LIST OF REFERENCES

1. Brooks, K. M., *An Investigation of Early Disturbances Found in Association with Laser-Produced Plasmas*, M.S. Thesis, Naval Postgraduate School, Monterey, California, December 1973.
2. Case, R. S., *An Investigation of Self-generated Magnetic Fields and Electron Emission in Laser Produced Plasmas*, Ph.D. Thesis, Naval Postgraduate School, Monterey, California, March 1974.
3. Polk, J. S., *Laser Induced Desorption of Gas from Stainless Steel Surfaces*, M.S. Thesis, Naval Postgraduate School, Monterey, California, June 1977.
4. Hawng, Z. W., *Laser Induced Evaporation from Stainless Steel and TiC Coated Surfaces*, M.S. Thesis, Naval Postgraduate School, Monterey, California, June 1980.
5. Travers, L. J., *A Model for Laser Produced Material Surface Evaporation*, M.S. Thesis, Naval Postgraduate School, Monterey, California, March 1980.
6. Keville, M. T. and Lautrup, R. W., *An Investigation of Unipolar Arcing Damage on Stainless Steel and TiC Coated Surfaces*, M.S. Thesis, Naval Postgraduate School, Monterey, California, June 1980.
7. Schwirzke, F. and Taylor, R. J., "Surface Damage by Sheath Effects and Unipolar Arcs," *Journal of Nuclear Materials*, v. 93 and 94, pp. 780-784, 1980.
8. Hoover, T. J., *An Investigation of Unipolar Arcing in Conductors and Metallic Glasses*, M.S. Thesis, Naval Postgraduate School, Monterey, California, September 1981.
9. Ryan, F. T. and Shedd, S. T., *A Study of the Unipolar Arcing Damage Mechanism on Selected Conductors and Semiconductors*, M.S. Thesis, Naval Postgraduate School, Monterey, California, June 1981.
10. Beelby, M. H., and Ulrich, H. G., *A Study of the Breakdown Mechanism of AISI 304 SS, AISI 2024 Aluminum and Various Titanium Coatings*, M.S. Thesis, Naval Postgraduate School, Monterey, California, December 1981.
11. Metheny, R. M., *An Investigation of Energy Coupling in Various Arc Susceptible and Resistant Conductors*, M.S. Thesis, Naval Postgraduate School, Monterey, California, June 1982.
12. Jenkins, W. F. and Schmidt, W. R., *Thermal Coupling and Damage Mechanisms of 1.06 Micron Laser Radiation and Laser Produced Plasma on Selected Materials*, M.S. Thesis, Naval Postgraduate School, Monterey, California, December 1982.
13. Stephenson, C. O., *Laser Damage to Spherical Targets*, M.S. Thesis, Naval Postgraduate School, Monterey, California, June 1985.

14. Olson, J. S., *CO<sub>2</sub> Pulsed Laser Damage Mechanisms and Assessment of Plasma Effects (Unfocused Beam)*, M.S. Thesis, Naval Postgraduate School, Monterey, California, December 1986.
15. Naval Postgraduate School Report NPS-61-83-008, *Unipolar Arcing, A Basic Laser Damage Mechanism*, by F. Schwirzke, 5 May 1983.
16. Robson, A. E. and Thonemann, P. C., "An Arc Maintained on an Isolated Metal Plate Exposed to a Plasma," *Procedural Physics Society*, v. 73, pp. 508-512, 1959.
17. Behrisch, R., "Surface Erosion from Plasma Materials Interaction," *Journal of Nuclear Materials*, v. 85 and 86, pp. 1047-1061, 1979.
18. Ready, John F., *Industrial Applications of Lasers*, Academic Press, 1978.
19. Chen, Francis F., *Introduction to Plasma Physics and Controlled Fusion*, v 1, 2nd edition, Plenum Press, 1984.
20. Naval Postgraduate School Report NPS-61-82-002, *Basic Mechanisms that Lead to Laser Damage*, by F. Schwirzke, M. H. Beelby, and H. G. Ulrich, 5 October 1981.
21. Air Force Weapons Laboratory Report AFWL-TR-73-92 *Explosive Electron Emission and the Characteristics of High-Current Electron Flow*, by R. K. Parker, pp. 17-74, February 1974.
22. Brooks, D. L., "NRL Plasma Formulary," Naval Research Laboratory, 1980.
23. Miller, R. B., *An Introduction to the Physics of Intense Charged Particle Beams*, Plenum Press, 1982.
24. Halbritter, J., "Dynamical Enhanced Electron Emission and Discharges at Contaminated Surfaces," *Applied Physics A*, v. 39, pp. 49-57, 1986.
25. Patel, C. K. N., "High Power Carbon Dioxide Lasers," *Scientific American*, pp. 264-275, August 1968.
26. Lumonics Inc., *Instruction Manual, Lumonics TE-820 HP CO<sub>2</sub> Laser*, 1976.
27. Belforte, David and Levitt, Morris, *The Industrial Laser Annual Handbook*, 1986 edition, v. 629, pp. 38-55, Pen Well Publishing Company, 1986.
28. Holman J. P., *Experimental Methods for Engineers*, 3rd ed., pp. 44-51, McGraw-Hill Book Company, 1978.
29. Peckner, D. and Bernstein, I. M., *Handbook of Stainless Steels*, McGraw-Hill Book Company, 1977.



# INITIAL DISTRIBUTION LIST

	No. Copies
1. Defense Technical Information Center Cameron Station Alexandria, Virginia 22304-6145	2
2. Library, Code 0142 Naval Postgraduate School Monterey, California 93943-5002	2
3. Professor F. R. Schwirzke, Code 61Sw Department of Physics Naval Postgraduate School Monterey, California 93943-5000	2
4. Distinguished Professor Alan E. Fuhs Code 72 Naval Postgraduate School Monterey, California 93943-5000	1
5. Department Chairman Department of Physics Naval Postgraduate School Monterey, California 93943-5000	1
6. Plasma Physics and Laser Laboratory Spanagel Hall (Bldg. 232, Rm. 27) Naval Postgraduate School Monterey, California 93943-5000	2
7. Commander John S. Olson SPC-30 Polaris Missile Facility Atlantic Charleston, South Carolina 29408-5700	1
8. Lieutenant Richard L. Weston Class 97 Surface Warfare Office School Newport, Rhode Island 02841	2

18070 2







DUDLEY KNOX LIBRARY  
NAVAL POSTGRADUATE SCHOOL  
MONTREY, CALIFORNIA 93943-5002

Thesis  
W484235 Weston  
c.1 CO<sub>2</sub> pulsed laser da-  
mage mechanism and plas-  
ma effects (focused  
bean).

Thesis  
W484235 Weston  
c.1 CO<sub>2</sub> pulsed laser da-  
mage mechanism and plas-  
ma effects (focused  
bean).

DUDLEY KNOX LIBRARY



3 2768 00018116 8